

## Master Thesis

*For obtaining the academic degree Diplom-Ingenieur*

*Masters Program Pharmaceutical Engineering*

# Mixing and Dissolution Processes - Investigation of Physicochemical Properties

Martina Gsöll, BSc

January 2011



*Advisors:*

**Univ.-Prof. Dr.techn. Dipl.-Ing. Johannes G. Khinast**

Institute for Process and Particle Engineering, University of Technology, Graz

**Dipl.-Ing. Dr.-Ing. Daniele Suzzi**

**Dipl.-Ing. Thomas Hörmann**

Research Center Pharmaceutical Engineering GmbH, Graz

---

Deutsche Fassung:  
Beschluss der Curricula-Kommission für Bachelor-, Master- und Diplomstudien vom 10.11.2008  
Genehmigung des Senates am 1.12.2008

## EIDESSTÄTLICHE ERKLÄRUNG

Ich erkläre an Eides statt, dass ich die vorliegende Arbeit selbstständig verfasst, andere als die angegebenen Quellen/Hilfsmittel nicht benutzt, und die den benutzten Quellen wörtlich und inhaltlich entnommene Stellen als solche kenntlich gemacht habe.

Graz, am .....

.....  
(Unterschrift)

Englische Fassung:

## STATUTORY DECLARATION

I declare that I have authored this thesis independently, that I have not used other than the declared sources / resources, and that I have explicitly marked all material which has been quoted either literally or by content from the used sources.

.....  
date

.....  
(signature)

# Acknowledgment

First of all I want to thank my advisor Univ.-Prof. Dipl.-Ing. Dr.techn. Johannes G. Khinast and the Research Center Pharmaceutical Engineering GmbH who offered me the possibility to write this thesis. Further thanks go to Dipl.-Ing. Dr.-Ing. Daniele Suzzi for his guidance and supervision throughout my work and to Dipl.-Ing. Thomas Hörmann who assisted and supported me to the best of his knowledge.

I am very thankful to my colleagues and staff in the laboratory, most of all Johannes Hofer, BSc and Dipl.-Ing. Dr.techn. Heidi Gruber-Wölfler who provided their kind support and assistance throughout my experimental research and work.

Thanks also go to Dipl.-Ing. Nikolaus Balak and Dipl.-Ing. Otto Scheibelhofer who helped and assisted me in evaluating the experimental data and supported me in realizing this work using  $\text{\LaTeX}$ .

My deepest gratitude goes to my parents and my sister Barbara for their support, understanding and constant encouragement throughout my studies. I want to dedicate this thesis to my colleague and friend Silvia Larisegger who was a permanent companion in my years of study and encouraged and motivated me whenever needed.

# Abstract

The dissolution of powders in liquids represents a process of particular importance in the pharmaceutical industry. Some examples for such applications are homogenization, suspending finely divided solid particles in liquids and the manufacturing of solutions and pre-mixes. In order to understand and characterize the mass transfer phenomena between bulk material and buffer liquid, a model system of polyethylene glycol (PEG) in water was analyzed.

First, the physicochemical properties of the powder were investigated experimentally, namely the particle size distribution, the particle shape and the specific surface area of the particles. The powder bulk properties were analyzed by rheological tests. This was performed using powder samples with distinct particle size distributions, which were obtained by milling.

Since high concentrated PEG-solutions lead to highly viscous liquids, fluid properties like density, viscosity and the saturation concentration were examined as well.

To gain insight into the dissolution kinetics of PEG in water, the powder was then fed and dissolved into a lab-scale stirred tank. Meanwhile, the time evolution of concentration was measured using midinfrared (MIR) spectroscopy techniques. In order to find a correlation between powder properties and dissolution behavior, the same experiments were carried out using PEG particles with different particle size and varying impeller speed. Other parameters like temperature and feeding rate were kept constant during all tests.

Based on these studies, a mathematical model was developed to describe the dissolution process. In addition, the results from the rheological tests were used for the design of a hopper, to calculate the critical conus angle and hopper outlet size.

The analysis of particle and powder attributes resulted in a decrease of particle size and polydispersity with increasing milling duration. Simultaneously, the specific surface area and the pore volume of the grains increased with decreasing particle size.

The PEG in water solutions showed a linear increase of the density and an exponential rise of the dynamic viscosity with increasing concentration of PEG.

---

From the dissolution experiments a correlation between particle size and dissolution rate was observable. Faster dissolution behavior of smaller particles was, at least at higher concentration and therefore higher viscosity of the solutions, proofed.

The final outcome of this work was a precise characterization of the bulk powder feeding and dissolution process, as well as a deep understanding of the effects of physicochemical properties on the overall process quality.

# Kurzfassung

Das Lösen und Mischen von Feststoffen in Flüssigkeiten spielt eine große Rolle in der pharmazeutischen Industrie. So sind beispielsweise die Herstellung von Suspensionen und Lösungen sowie Homogenisierungsvorgänge wichtige Prozessschritte. Um diese zu optimieren, ist es notwendig, die physikalisch-chemischen Eigenschaften des Feststoffes und des Lösungsmittels, wie zum Beispiel Partikelgröße, -form, Viskosität und Dichte, zu kennen.

In dieser Arbeit wurde hierfür ein Modell-System, bestehend aus Polyethylenglykol (PEG) und Wasser, verwendet um oben genannte physikalisch-chemische Eigenschaften näher zu untersuchen. PEG wurde hinsichtlich Partikelgröße, -form und spezifischer Oberfläche analysiert. Außerdem erfolgte eine Charakterisierung der Pulvereigenschaften des Schüttgutes mittels rheologischer Tests. Um den Einfluss der Partikelgröße auf vorhin genannte Parameter festzustellen, wurden die Partikel mit Hilfe einer Kugelmühle zerkleinert und dieselben Messungen wiederholt. Ebenso wurden Dichte, Viskosität und Sättigungskonzentration der Lösungen bestimmt.

Um weitere Aussagen über die Lösungseigenschaften zwischen Fest- und Flüssigphase (Lösekinetik, Stofftransport) von PEG in Wasser zu treffen, wurden Löseversuche in einem Rührtank durchgeführt. Hierfür wurde PEG mit Hilfe einer Vibrorinne in Wasser zudosiert und die Konzentrationsänderung der Lösung mittels einer Mittelinfrarot (MIR) Sonde verfolgt. Um eine Abhängigkeit zwischen Lösegeschwindigkeit und Partikelgröße zu finden, wurden für die Versuche PEG-Pulver mit unterschiedlichen Partikelgrößen verwendet. Ebenso wurde die Rührgeschwindigkeit variiert, wogegen Parameter wie Temperatur und Dosierate konstant gehalten wurden.

Um den Löseprozess zu charakterisieren und die experimentellen Daten zu validieren, erfolgte die Erstellung eines einfachen mathematischen Modells. Die Ergebnisse aus den rheologischen Messungen wurden verwendet, um die kritische Auslaufgeometrie einer Dosiereinheit zu berechnen.

---

Folgende Resultate konnten aus den Experimenten erzielt werden: aus der Charakterisierung der Pulver-Eigenschaften ergab sich wie erwartet eine Abnahme der Partikelgröße und Polydispersität mit zunehmender Mahldauer. Gleichzeitig konnte die Zunahme der spezifischen Oberflächen und Porenvolumina der Proben mit abnehmender Partikelgröße bestätigt werden.

Die Untersuchungen der Lösungseigenschaften zeigten einen linearen Anstieg der Dichte und eine exponentielle Zunahme der Viskosität mit zunehmender Konzentration der Lösungen.

Ebenso konnte aus den Löseversuchen ein Zusammenhang zwischen Partikelgröße und Lösegeschwindigkeit beobachtet werden. Das Lösen kleiner Partikel erfolgte, zumindest bei hohen Konzentrationen und somit hoher Viskosität der PEG-Lösungen, schneller und führte somit zu höheren Löseraten.

# Contents

|   |            |
|---|------------|
| <b>Acknowledgment</b>   | <b>i</b>   |
| <b>Abstract</b>   | <b>ii</b>  |
| <b>Kurzfassung</b>  | <b>iv</b>  |
| <b>List of Tables</b>   | <b>ix</b>  |
| <b>List of Figures</b>  | <b>xi</b>  |
| <b>Abbreviations</b>  | <b>xiv</b> |
| <b>1. Goals and Motivation</b>  | <b>1</b>   |
| <b>2. Process Description</b>   | <b>3</b>   |
| 2.1. Feeding: Powder Flow and Storage . . . . .                         | 4          |
| 2.1.1. Particle Attributes . . . . .                                    | 5          |
| 2.1.2. Powder Attributes and Dynamics . . . . .                         | 8          |
| 2.1.3. Equipment Properties and Hopper Design . . . . .                 | 14         |
| 2.2. Dissolution . . . . .  | 18         |
| 2.2.1. Dissolution Process . . . . .                                    | 18         |
| 2.2.2. Dissolution and Mass Transfer in Solid-Liquid Systems . . . . .  | 20         |
| 2.3. Mixing and Homogenization . . . . .                                | 24         |
| 2.3.1. Process Parameters . . . . .                                     | 24         |
| 2.3.2. Hydrodynamics of Solid Suspension and Distribution . . . . .     | 25         |
| 2.3.3. Selection and Design Issues for Solid-Liquid Equipment . . . . . | 28         |
| <b>3. Experimental Procedure</b>  | <b>32</b>  |
| 3.1. Design of Experiment . . . . .                                     | 32         |
| 3.2. Analysis of Bulk and Particle Properties . . . . .                 | 33         |
| 3.2.1. Variation of Particle Size by Milling . . . . .                  | 34         |

---

|           |  |           |
|-----------|--|-----------|
| 3.2.2.    | Particle Shape . . . . .                       | 36        |
| 3.2.3.    | Particle Size Distribution . . . . .           | 36        |
| 3.2.4.    | Particle Surface Area . . . . .                | 37        |
| 3.2.5.    | Powder Rheology . . . . .                      | 38        |
| 3.3.      | Dissolution Experiments . . . . .              | 39        |
| 3.3.1.    | Dissolution in a Lab-Scale Tank . . . . .      | 39        |
| 3.4.      | Analysis of Solution Properties . . . . .      | 41        |
| 3.4.1.    | Density . . . . .                              | 42        |
| 3.4.2.    | Viscosity . . . . .                            | 42        |
| 3.4.3.    | Saturation Concentration . . . . .             | 42        |
| <b>4.</b> | <b>Results and Discussion</b>                  | <b>43</b> |
| 4.1.      | Analysis of Powder Properties . . . . .        | 43        |
| 4.1.1.    | Milling of the Particles and PSD . . . . .     | 43        |
| 4.1.2.    | Shape Analysis . . . . .                       | 46        |
| 4.1.3.    | Surface Area . . . . .                         | 49        |
| 4.1.4.    | Powder Rheology . . . . .                      | 52        |
| 4.2.      | Dissolution Experiment . . . . .               | 54        |
| 4.2.1.    | Dissolution in a Lab-Scale Tank . . . . .      | 54        |
| 4.3.      | Analysis of Solution Properties . . . . .      | 58        |
| 4.3.1.    | Density . . . . .                              | 58        |
| 4.3.2.    | Viscosity . . . . .                            | 59        |
| 4.3.3.    | Saturation Concentration . . . . .             | 60        |
| <b>5.</b> | <b>Dissolution Model</b>                       | <b>61</b> |
| 5.1.      | Mass Transfer Equations . . . . .              | 61        |
| 5.2.      | Calculation of the Dissolution Model . . . . . | 64        |
| <b>6.</b> | <b>Hopper Design</b>                           | <b>70</b> |
| 6.1.      | Conus Angle . . . . .                          | 70        |
| 6.2.      | Hopper Outlet Size . . . . .                   | 71        |
| <b>7.</b> | <b>Conclusions</b>                             | <b>76</b> |
| <b>A.</b> | <b>Tables and Figures</b>                      | <b>79</b> |
| A.1.      | Particle Size Distribution . . . . .           | 79        |
| A.2.      | Powder Rheology . . . . .                      | 80        |
| A.2.1.    | Compressibility Test . . . . .                 | 80        |

|  |           |
|--|-----------|
| A.2.2. Wall Friction Test . . . . .                            | 80        |
| A.3. Dissolution Experiment . . . . .                          | 81        |
| A.3.1. Cleaning of the Probe . . . . .                         | 81        |
| A.3.2. Precision and Reliability of MIR Measurements . . . . . | 81        |
| A.4. Solution Properties . . . . .                             | 83        |
| A.4.1. Density . . . . .                                       | 83        |
| A.4.2. Viscosity . . . . .                                     | 84        |
| <b>Bibliography</b>  | <b>85</b> |

# List of Tables

|  |    |
|--|----|
| 2.1. Physical and external factors affecting the flowability of bulk material [10]. . . . .  | 8  |
| 2.2. Empirical and semi-empirical relations for calculating the Sherwood number. . . . .   | 22 |
| 3.1. Parameters for the dissolution experiments. . . . .   | 33 |
| 3.2. Sample labeling. . . . .  | 34 |
| 3.3. Parameter study for the ball mill - variations in filling capacity. . . . .   | 35 |
| 3.4. Parameter study for the ball mill - variation in grinding time. . . . .   | 35 |
| 4.1. Influence of filling capacity of the milling vessels on PSD. . . . .  | 44 |
| 4.2. Influence of grinding duration on PSD; filling capacity of 60 g. . . . .  | 44 |
| 4.3. Influence of grinding duration on PSD; filling capacity of 90 g. . . . .  | 45 |
| 4.4. Variations in particle size between 5 different batches of PEG milled for 3 and 10 minutes each. . . . .  | 45 |
| 4.5. Particle properties from <i>ASAP</i> measurements. . . . .  | 50 |
| 4.6. Compressibility indices and conditioned bulk densities of different lots of PEG. . . . .  | 53 |
| 4.7. Wall friction angles of different lots of PEG. . . . .  | 54 |
| 4.8. Analysis of the saturation concentration of PEG in water. . . . .   | 60 |
| 5.1. Dissolution times of Lot 3 and Lot 10. . . . .  | 67 |
| 6.1. Calculated conus angles for conical and plane flow hoppers. . . . .   | 71 |
| 6.2. Calculated dimensions of outlet sizes for conical and plane flow hoppers. . . . .   | 75 |
| A.1. Setting of parameters for QicPic analysis. . . . .  | 79 |
| A.2. Precision of the MIR measurements depending on the dissolution step, $c_t$ - target concentration, $c_a$ - averaged actual concentration. . . . .   | 81 |
| A.3. Reliability of the MIR measurements depending on the dissolution step, $c_t$ - target concentration, $c_a$ - averaged actual concentration. . . . . | 82 |

|   |    |
|---|----|
| A.4. Densities of the standard solutions of PEG in water. . . . . | 83 |
| A.5. Viscosity of the standard solutions of PEG in water. . . . . | 84 |

# List of Figures

|   |    |
|---|----|
| 2.1. Important operating units of a dissolution process: feeding, dissolution and homogenization [16]. . . . .  | 3  |
| 2.2. Factors influencing the performance of a solids processing unit according to Wibowo and Ng [43]. . . . .   | 4  |
| 2.3. (a) Liquid bridge between two spheres of equal size [37]; (b) different types of liquid bridges: a. pendular, b. funicular, c. capillary state [32]. | 6  |
| 2.4. Flow patterns occurring within a silo during discharge: mass flow (left) and funnel flow (right) [36]. . . . .                                       | 9  |
| 2.5. Horizontal, $\sigma_h$ , and vertical forces, $\sigma_v$ , acting on a bulk element [10]. . .  | 11 |
| 2.6. Triangular element of bulk solid (a) and stresses acting on it (b). . . . .  | 12 |
| 2.7. Analysis of forces using the Mohr Circle [34]. . . . .   | 13 |
| 2.8. Characteristic powder properties derived by Mohr Circle analysis [30]. .   | 14 |
| 2.9. Different styles of hoppers: conical, plane flow, transition, chisel, pyramid, square opening (from left to right) [10]. . . . .                     | 15 |
| 2.10. Powder Rheometer [10]. . . . .  | 16 |
| 2.11. Contact angles indicating different wettability. . . . .  | 19 |
| 2.12. Relative mass transfer as function of impeller power [26]. . . . .  | 23 |
| 2.13. States of solid suspensions: (a) partial (b) complete (c) uniform. . . . .  | 27 |
| 2.14. Characteristic dimensions of a stirred tank with dished bottom head [16].   | 29 |
| 2.15. Common glass-lined baffle types [26]. . . . .   | 29 |
| 2.16. (a) Hydrofoil turbine impeller and (b) close-clearance impellers: anchor (left) and helical ribbon (right) [26]. . . . .                            | 30 |
| 2.17. (a) Axial flow impeller: pitched blade turbine and (b) radial flow impeller: open flat blade [26]. . . . .  | 30 |
| 3.1. Diameter of a circle of equal projection area. . . . .   | 37 |
| 3.2. Lab-scale plant (a) and schematic description (b). . . . .   | 39 |
| 3.3. Peak area used for evaluation of spectral data. . . . .  | 41 |

---

|   |    |
|---|----|
| 4.1. Variations in particle size between 5 different batches of PEG milled for 3 and 10 minutes each. . . . .                                     | 46 |
| 4.2. PEG unground. . . . .  | 47 |
| 4.3. PEG ground for 3 minutes. . . . .  | 47 |
| 4.4. PEG ground for 5 minutes. . . . .  | 47 |
| 4.5. PEG ground for 7 minutes. . . . .  | 48 |
| 4.6. PEG ground for 10 minutes. . . . .   | 48 |
| 4.7. QicPic image analysis of PEG ground for 3 minutes (a) and 5 minutes (b). . . . .   | 49 |
| 4.8. QicPic image analysis of PEG ground for 7 minutes (a) and 10 minutes (b). . . . .  | 49 |
| 4.9. Specific surface area of 3 different lots of PEG. . . . .  | 50 |
| 4.10. Pore diameter of 3 different lots of PEG. . . . .   | 51 |
| 4.11. Total pore volume of 3 different lots of PEG. . . . .   | 51 |
| 4.12. Stability test for Lot native and Lot 10. . . . .   | 53 |
| 4.13. Calibration fit used for evaluation of spectral data. . . . .   | 55 |
| 4.14. Normalized dissolution profiles of steps 1-5; the solid line representing Lot 3, the dotted line Lot 10; impeller speed of 150 rpm. . . . . | 56 |
| 4.15. Dissolution profiles of Lot 3 and Lot 10 at 90 rpm. . . . .   | 57 |
| 4.16. Density of the PEG solutions. . . . .   | 59 |
| 4.17. Dynamic viscosity of the PEG solutions. . . . .   | 60 |
| 5.1. Characteristic length of a sphere to be overflowed by a fluid. . . . .   | 63 |
| 5.2. Decrease of particle diameter as a function of time. . . . .   | 64 |
| 5.3. Calculated dissolution profiles for Lot 3 and Lot 10. . . . .  | 67 |
| 5.4. Experimental (Exp.) and modelled (M.) dissolution profiles of Step 1 (left) and Step 2 (right). . . . .                                      | 68 |
| 5.5. Experimental (Exp.) and modelled (M.) dissolution profiles of Step 3 (left) and Step 4 (right). . . . .                                      | 69 |
| 5.6. Experimental (Exp.) and modelled (M.) dissolution profiles of Step 5. . . . .  | 69 |
| 6.1. Conus angle and hopper outlet size of a conical and a plane flow hopper [10]. . . . .  | 70 |
| 6.2. Hopper and powder flow functions for determination of critical stress developed within the powder [29]. . . . .                              | 73 |
| 6.3. Hopper flow functions and powder flow functions of Lot 3 and Lot 10. . . . .   | 74 |
| A.1. Compressibility of Lot native, Lot 3 and Lot 10. . . . .   | 80 |

---

|   |    |
|---|----|
| A.2. Steady-state shear stress against normal stress. . . . .   | 80 |
| A.3. Dissolution profiles of Lot 3-2 and Lot 10-2 at 150 rpm. . . . .   | 81 |
| A.4. Precision and trueness of MIR measurements. . . . .  | 82 |
| A.5. Reliability of MIR measurements; comparison of averaged actual and<br>target concentration of the PEG solutions. . . . . | 83 |

# Abbreviations

## Abbreviations

|      |                             |
|------|-----------------------------|
| ATR  | attenuated total reflection |
| BET  | Brunauer Emmett Teller      |
| Exp. | Experimental                |
| M.   | Model                       |
| MIR  | midinfrared                 |
| PEG  | polyethylene glycol         |
| PSD  | particle size distribution  |
| SIM  | sample interface module     |

## Nomenclature

|                  |   |
|------------------|---|
| $\dot{M}$        | mass flow of the particles [ $kg/s$ ]                           |
| $\overline{M}_t$ | averaged mass transfer [ $kg/s$ ]                               |
| $A$              | total surface area of the particle [ $m^2$ ]                    |
| $a$              | distance between particles [ $m$ ]                              |
| $B$              | critical diameter of the outlet of a hopper [ $m$ ]             |
| $B_c$            | critical diameter of the outlet of a conical hopper [ $m$ ]     |
| $B_p$            | critical outlet size of a plane flow hopper [ $m$ ]             |
| $BFE$            | basic flowability energy [ $mJ$ ]                               |
| $C$              | impeller to tank bottom clearance [ $m$ ]                       |
| $c_{end}$        | end-concentration of homogeneous solution [ $wt.\%$ ]           |
| $C_H$            | Hamaker constant [ $J$ ]  |
| $c_t$            | actual concentration of the solution at time step t [ $wt.\%$ ] |
| $CI$             | compressibility index [-]                                       |
| $D$              | bulk diffusion coefficient [ $m^2/s$ ]                          |
| $d$              | diameter of the impeller blades [ $m$ ]                         |
| $d_p$            | particle diameter [ $\mu m$ ]                                   |
| $EQPC$           | diameter of a circle of equal projection area [ $\mu m$ ]       |
| $F_{el}$         | electrostatic force [ $N$ ]                                     |

---

|               |  |
|---------------|--|
| $F_{vdW}$     | van der Waals force [ $N$ ]  |
| $ff$          | hopper flow factor [-]   |
| $g$           | acceleration due to gravity [ $m/s^2$ ]  |
| $H$           | liquid depth in a stirred vessel [ $m$ ]   |
| $h\omega$     | Lifschitz- Van der Waals constant [ $Nm$ ]   |
| $H(\Theta)$   | factor determined by the slope of the hopper wall [-]                                |
| $H_c(\Theta)$ | factor determined by the slope of the hopper wall, conical hopper [-]                |
| $H_p(\Theta)$ | factor determined by the slope of the hopper wall, plane flow hopper [-]             |
| $L'$          | characteristic length of the body to be overflowed [ $m$ ]                           |
| $M_a$         | average molecular weight [ $g/mol$ ]   |
| $m_{p0}$      | primary particle mass added to the solution [ $kg$ ]                                 |
| $m_{pt}$      | mass of particles being dissolved at time step t [ $kg$ ]                            |
| $MPS$         | major principal or consolidation stress [kPa]  |
| $n$           | rotation speed of the impeller [ $rpm$ ]   |
| $N_{js}$      | minimum agitation speed to attain complete suspension [ $rpm$ ]                      |
| $Re$          | Reynolds number [-]  |
| $Re_p$        | particle Reynolds number [-]   |
| $S$           | dimensionless particle suspension parameter [-]                                      |
| $Sc$          | Schmidt number [-]   |
| $Sh$          | Sherwood number [-]  |
| $SI$          | stability index [-]  |
| $T$           | vessel diameter [ $m$ ]  |
| $U$           | circumference of a particle orthogonal to the flow direction of the fluid [ $m$ ]    |
| $U_c$         | contact potential of conductors [ $V$ ]  |
| $UYS$         | unconfined yield strength [ $kPa$ ]  |
| $v$           | mean fluid velocity [ $m/s$ ]  |
| $v_{rel}$     | relative velocity between the fluid and the particles [ $m/s$ ]                      |
| $V_t$         | free settling velocity of particles [ $m/s$ ]  |
| $X$           | initial solids mass fraction [ $wt.\%$ ]   |
| $x_{10}$      | particle size, where 10 % of the total quantity of particles are smaller [ $\mu m$ ] |
| $x_{50}$      | particle size, where 50 % of the total quantity of particles are smaller [ $\mu m$ ] |
| $x_{90}$      | particle size, where 90 % of the total quantity of particles are smaller [ $\mu m$ ] |
| $x_{max}$     | maximum diameter of the particles [ $\mu m$ ]  |
| $x_Q$         | characteristic particle size for a given Q-value [ $\mu m$ ]                         |
| $z_p$         | number of particles [-]  |

**Greek**

|                   |   |
|-------------------|---|
| $\beta$           | mass transfer coefficient [ $m/s$ ]                                     |
| $\delta$          | bridge angle [ $^{\circ}$ ]   |
| $\gamma$          | surface tension [ $N/m$ ]   |
| $\gamma_{LV}$     | interfacial tension liquid-vapor [ $N/m$ ]                              |
| $\gamma_{SL}$     | interfacial tension solid-liquid [ $N/m$ ]                              |
| $\gamma_{SV}$     | interfacial tension solid-vapor [ $N/m$ ]                               |
| $\mu$             | dynamic viscosity [ $mPa \cdot s$ ]                                     |
| $\nu$             | kinematic viscosity [ $m^2/s$ ]   |
| $\rho^*$          | density of the saturated solution [ $kg/m^3$ ]                          |
| $\rho^{\infty}$   | local density of the solution [ $kg/m^3$ ]                              |
| $\rho_{B,crit}$   | critical bulk density [g/ml]  |
| $\sigma_{\alpha}$ | normal stress acting on a plane inclined by an angle $\alpha$ [ $kPa$ ] |
| $\sigma_c$        | compacting stress in a hopper [ $kPa$ ]                                 |
| $\sigma_D$        | stress developed within the powder [ $kPa$ ]                            |
| $\sigma_y$        | unconfined yield strength [ $kPa$ ]                                     |
| $\tau_0$          | cohesion [ $kPa$ ]  |
| $\tau_{\alpha}$   | shear stress acting on a plane inclined by an angle $\alpha$ [ $kPa$ ]  |
| $\theta$          | contact angle [ $^{\circ}$ ]  |
| $\Theta$          | conus angle [ $^{\circ}$ ]  |
| $\Theta_c$        | conus angle for cylindrical hoppers [ $^{\circ}$ ]                      |
| $\Theta_p$        | conus angle for plane flow hoppers [ $^{\circ}$ ]                       |
| $\varepsilon$     | relative permittivity [-]   |
| $\varepsilon_0$   | permittivity of free space [ $As/Vm$ ]                                  |
| $\varphi_e$       | effective angle of internal friction [ $^{\circ}$ ]                     |
| $\varphi_i$       | angle of internal friction [ $^{\circ}$ ]                               |
| $\varphi_w$       | angle of wall friction [ $^{\circ}$ ]                                   |
| $\rho_L$          | density of the liquid [ $kg/m^3$ ]                                      |
| $\rho_S$          | density of the solid [ $kg/m^3$ ]                                       |

# 1. Goals and Motivation

The dissolution of powders in liquids is an important process for many sectors of industry but also comes across in every day life. For example, the dispersion and dissolution of whole milk powder, powdered instant beverages like cocoa, or even the dissolution of active pharmaceutical components like effervescent tablets or powder prior to consumption are well known applications [11, 25]. In terms of industry, the procedure of dissolving a powder in a liquid can be found in various branches: starting from food industry, cosmetics and consumer products, chemicals, pharmaceuticals, biotechnology, agrochemicals up to polymer processing, paints and automotive finishes, pulp and paper and mineral processing [26]. For example, the dispersion of fine pigments to obtain colors and paints is a challenging task, as the product has to be homogeneous and stable. In addition to dispersion and dissolution of a powder into a liquid to gain homogeneous solutions, the precedent feeding procedure is of great significance as well. In order to characterize the dissolution process, a deep understanding of its operating mode, thus of all parameters and external factors involved, is crucial. Therefore, it is important to focus on its three distinct operating units: *feeding*, *dissolution* and *homogenization/mixing*.

A lot of research has been done in the last years in the field of dissolution and mixing processes. Freudig et al. [11] investigated the dispersion of powders in liquids in a stirred vessel considering the importance of wettability on the process. Another work was done by Hoge Kamp and Pohl [14] who focused on the evaluation of the wetting and dispersion characteristics of powders. In the area of food industry, the instantization of powders plays a major role on the dissolution and dispersion behavior and was the object of investigation by Schubert [33].

In this study, a model system consisting of PEG in water was created and characterized. The attention was in particular turned on the investigation of the physicochemical properties of powder and solution, as well as on their influence on the dissolution

---

process. Bulk properties like particle shape, particle size distribution (PSD), particle surface and powder rheology were experimentally assessed. Thereafter, the powder was fed into a lab-scale stirred tank to gain insight into the dissolution kinetics. Here, the influence of particle size and impeller speed on dissolution time was evaluated. Therefore, the bulk material was milled to obtain smaller particles and the same tests were repeated. The data from the experiments were then used to develop a mathematical model for understanding and characterizing the mass transfer phenomena between the bulk material and the liquid. In addition, the results from the rheological tests were taken to design a hopper and to calculate the critical conus angle and hopper outlet size, respectively.

The experimental characterizations were carried out with the following equipment:

- *QicPic Image Analysis System* by *Sympatec* to determine particle size and shape;
- *Leica DM 4000 microscope* for particle shape analysis;
- *Micromeritics ASAP 2010* to assess the specific surface area of the particles;
- *FT4 Powder Rheometer* by *Freeman Technologies* to characterize powder and bulk properties;
- *ATR-FTIR Spectroscopy System* by *Mettler Toledo* for measuring the concentration of PEG in water solutions;
- *Anton Paar Stabinger Viscometer SVM 3000* for analysis of density and viscosity of the solutions

In summary, the following goals were aspired in this work:

- to define and measure the critical physicochemical properties of a bulk material to be fed and dissolved into a stirred tank;
- to assess the impact of different input parameters, like PSD and impeller speed on the dissolution behavior of the fed powder;
- to generate a mathematical model to describe and predict the dissolution behavior;
- to design the feeding equipment according to powder rheology data.

## 2. Process Description

Dissolution and dispersion of solids in liquids is a complex industrial process, which consists of several single operating units being influenced by a great number of parameters. In order to characterize and optimize the dissolution procedure, we concentrate on three important unit operations, namely *feeding*, *dissolution* and *homogenization* (see Figure 2.1):

**Feeding** The feeding system is affected by the flow behavior of the bulk material, by powder properties like particle shape, size, surface area, density, porosity etc., but also by external factors like moisture level, storage time, air content and the material properties of the feeding device [10].

**Dissolution** Several particle properties like size, shape, surface and wetting characteristics influence the dissolution behavior of a powder, but also process parameters like impeller speed, temperature and feeding rate have a great impact on dissolution.

**Homogenization and Mixing** Considering homogenization and mixing, it is fundamental to have in mind fluid properties like density and viscosity, operating conditions like temperature and impeller speed, but also equipment parameters and design issues like baffles, geometry of the vessel and the stirrer.

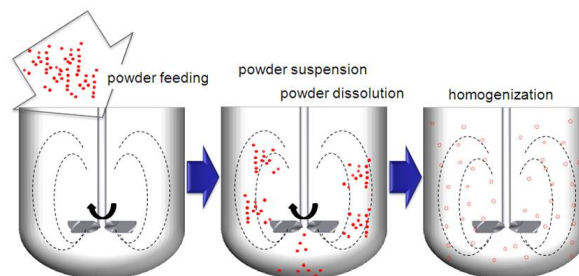


Figure 2.1.: Important operating units of a dissolution process: feeding, dissolution and homogenization [16].

For each of these three operating units the process parameters and the material attributes, mostly affecting the process, will be analyzed in the following sections.

## 2.1. Feeding: Powder Flow and Storage

Granular material, consisting of a large number of discrete solid particles, shows many unusual kinds of behavior and can be considered as an extraordinary state of matter because it can not be classified as either solids or liquids [17]. Therefore, the prediction of flow behavior in industrial applications is fundamental in order to prevent or avoid upcoming problems during storage and feeding. This implies that a detailed understanding of the powder bulk properties as well as its flowability and processability characteristics is needed to design and realize an equipment for processing solids [9]. Thus, the effects of material properties, operating conditions, particle attributes and inter-particle forces on powder behavior need to be analyzed in detail [43]. The influence and relationship of these factors on the performance of a solids processing unit of a single process was summarized by Wibowo and Ng [43] and is illustrated in Figure 2.2 :

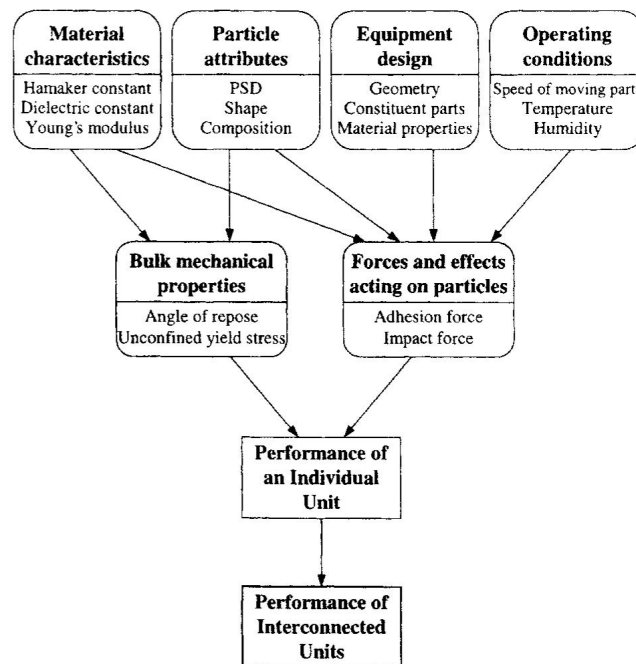


Figure 2.2.: Factors influencing the performance of a solids processing unit according to Wibowo and Ng [43].

### 2.1.1. Particle Attributes

#### Particle Size and Shape

Particle behavior is strongly influenced by size and shape of the particles. Bulk material properties and also forces acting on particles basically depend on these two magnitudes. Strong variations in particle size are the source for many problems occurring during processing solids like *segregation* and *agglomeration* (see section 2.1.2).

For example, in-bin segregation may lead to product inhomogeneity after discharge and the formation of aggregates or crusts may block the outlet of a hopper leading to production stoppages [43].

As almost no particles are perfect spheres, the shape also has a huge impact on particle behavior, bulk properties and powder dynamics, respectively. A vast number of particles are plates, needles, cubes, flakes, etc., therefore show *anisotropic* behavior [20]. This may lead to variations in bulk density, thus cause mechanical interlocking resulting in flow and processing problems.

Concluding, particle size and shape are of great importance with regard to ideal operating conditions and may not be neglected when constructing a solids processing plant.

#### Cohesive Forces between Particles

Considering the interactions between solid particles in a gaseous phase, one can distinguish between three kinds of cohesive forces, that become more important moving towards small scales [37]:

1. Capillary forces
2. Van der Waals forces
3. Electrostatic forces

##### 1. Capillary Forces

Liquids in contact with particle surfaces lead to the formation of bridges between neighboring elements. As a consequence, the particles are held together due to capillary forces. Depending on the amount of liquid phase, one can distinguish between the pendular, funicular and capillary state (see Figure 2.3(b)).

The force responsible for capillary binding consists of two components: the surface tension force and the force arising from the pressure difference inside and outside of

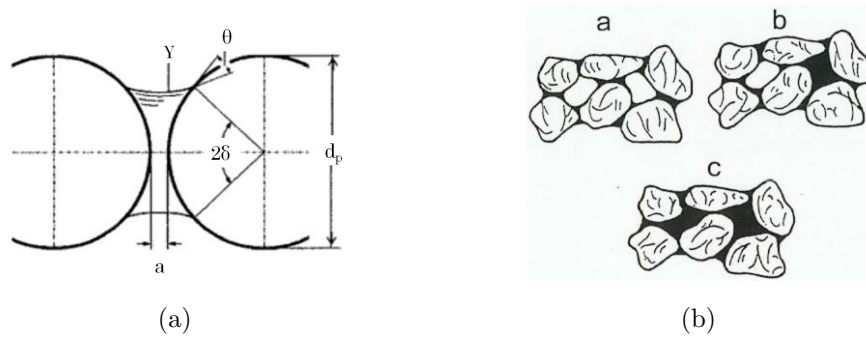


Figure 2.3.: (a) Liquid bridge between two spheres of equal size [37]; (b) different types of liquid bridges: a. pendular, b. funicular, c. capillary state [32].

the bridge [31]. These forces between particles depend on geometric properties like the distance between the particles  $a$ , the particle diameter  $d_p$ , the bridge angle  $\delta$ , as well as material properties like surface tension  $\gamma$  of the liquid and contact angle  $\theta$  [37].

If the amount of water between the particles is too high, the particles are not held together anymore.

## 2. Van der Waals Forces

Van der Waals forces arise from the dipole interactions between atoms and molecules of the particles. They act only within small distances and can be divided into three different types [38]: Keesom, Debye and London forces:

- *Keesom* forces: occurring between two permanent dipoles.
- *Debye* forces: arising between a permanent and an induced dipole.
- *London* forces: also referred to as dispersion forces, appearing between two induced dipoles. These forces stem from the natural oscillations of the electron clouds of the molecules that induce a dipole moment in the neighboring molecule [38].

For calculating the Van der Waals forces between two spheres of equal size, two different approaches are known [41]:

**Hamaker Theory.** The interacting forces between two particles are added, whereas the influence of neighboring atoms and molecules is disregarded. The Van der Waals force  $F_{vdW}$  can then be calculated according to

$$F_{vdW} = \frac{C_H \cdot d_p}{24 \cdot a^2} \quad (2.1)$$

where  $C_H$  is the Hamaker constant,  $d_p$  is the particle diameter and  $a$  is the distance between the particles. The Hamaker constant can be estimated from the dielectric properties of the materials involved and indicates attractive behavior if  $C_H > 0$ , while repulsive if  $C_H < 0$  [29].

**Lifschitz Theory.** In this approach, the interacting forces are calculated as a function of the dielectric constants of the participating molecules. Hence, the influence of neighboring atoms and molecules is incorporated. Following equation is used for calculating the Van der Waals  $F_{vdW}$  forces according to Lifschitz theory

$$F_{vdW} = \frac{h\omega \cdot d_p}{32 \cdot \pi \cdot a^2} \quad (2.2)$$

where  $h\omega$  is the Lifschitz-Van der Waals constant.

### 3. Electrostatic Forces

Electrostatic forces emerge between particles with charged surfaces. Among conductive materials this happens through electron transfer, whereas among insulators friction or attrition is responsible for charging of the material. The electrostatic force  $F_{el}$  between two spheres is given by

$$F_{el} = \frac{\pi}{4} \cdot \varepsilon_0 \cdot \varepsilon \cdot U_c^2 \cdot \frac{d_p}{a} \quad (2.3)$$

where  $\varepsilon_0$  is the permittivity of free space ( $\varepsilon_0 = 8.855 \cdot 10^{-12} \text{As/Vm}$ ),  $\varepsilon$  is the relative permittivity ( $\varepsilon = 1.00054$  for vacuum) and  $U$  is the contact potential of conductors (typical values are 0.1 - 0.7 V)[37].

*Note: Equations 2.1, 2.2 and 2.3 are only valid for spheres that are perfectly plane, clear and located to each other at a distance between 4 Å and 500 Å [37].*

## 2.1.2. Powder Attributes and Dynamics

### Powder Flow

Powder flow is a multidimensional and complex phenomenon depending on a vast number of parameters. The flowability of granular matter is affected by the physical properties of the bulk material, but also by external factors like e.g., moisture levels or the equipment used for processing and handling. Therefore, powder rheological investigations are a useful tool for identifying characteristic flow, shear and bulk properties. The most important factors affecting flowability, both physical and external, are displayed in Table 2.1.

| Physical factors           | External factors |
|----------------------------|------------------|
| Particle size distribution | Consolidation    |
| Particle shape             | Aeration         |
| Surface area               | Flow rates       |
| Density                    | Moisture levels  |
| Hygroscopicity             | Storage times    |
| Porosity                   | Electrostatics   |
| Surface texture            |                  |

Table 2.1.: Physical and external factors affecting the flowability of bulk material [10].

### Flow Profiles within a Hopper

Powders stored in a hopper undergo different flow patterns during discharge. Two characteristic types of flow profiles are commonly known, see Figure 2.4:

#### 1. Mass Flow

Mass flow occurs if all the powder is in motion and no stagnant regions appear within the silo. Material from the center, as well as from regions close to the hopper walls, flows out of the bin simultaneously. This leads to an uniform and well controlled flow pattern. Mass flow also results in a *"first in - first out flow sequence"*, which assures short residence times of the bulk material in the bin. Other advantages of this flow pattern are the reduction of segregation and a constant bulk density independent of the location within the hopper. However, one disadvantage is to be mentioned: particles

moving along the hopper walls may cause erosion of the wall material due to friction, thus lead to contaminations and impurities of the bulk material. [27, 29]

## 2. Funnel Flow

Funnel flow develops if only the bulk material in the center of a hopper, directly above the orifice, is in motion and forms a channel where powder flows. In the stagnant regions close to the hopper walls, termed "dead-zones", no motion occurs [19]. The resulting flow behavior of funnel flow is known as "*first in - last out flow sequence*" and may lead to stationary parts of the bulk, which do not discharge at all. Hence, this kind of flow behavior should be avoided.

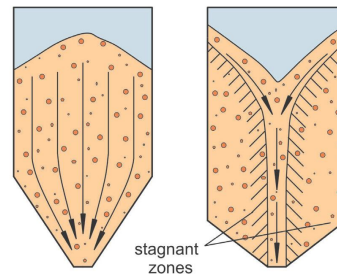


Figure 2.4.: Flow patterns occurring within a silo during discharge: mass flow (left) and funnel flow (right) [36].

## Problems Occurring during Processing Bulks

Handling and storage of granular materials is a field of particular interest in many sectors of industry, due to numerous problems that are often underestimated and can at worst lead to production stoppages [29]. Common problems occurring during feeding powders are:

**Arching.** Arching denotes the formation of a stable bridge above the outlet of the hopper and prevents discharge of the powder. Among fine and cohesive particles, arching occurs due to adhesive forces between the particles, whereas among coarse and non-cohesive particles this phenomenon results from wedging and interlocking of single grains. [19]

**Rat Holing or Piping.** These terms refer to the formation of a cavity or pipe above the outlet of the hopper [27]. Close to the walls, stagnant dead zones are built,

where no powder flow occurs. The appearing funnels can differ in symmetry depending on the powder properties of the bulk material, which may change by varying environmental conditions like e.g. humidity [19].

**Flooding.** Large amounts of air entrained in the bulk material can lead to fluidization of the granular material, resulting in an uncontrollable powder flow, also known as flooding [43]. This phenomenon occurs e.g. when a rat hole collapses [27].

**Attrition** Attrition describes the formation of small, ultrafine particles and is the result of internal or external changes, e.g. phase changes, vaporization of liquid into the particle or mechanical friction between particles or particles and walls. These variations in particle size affect the bulk properties and thereafter have a strong impact on further operations like mixing, storage and sieving [19].

**Segregation.** A mixture of bulk material never consists of particles which all have the same properties. Even if it is well blended, different particle attributes as well as processing and handling (e.g. moving, pouring or conveying) may evoke segregation. Variations in powder particle size, density or shape can lead to segregation, which results in inhomogeneity of powder and particle properties within the hopper [19].

Differences in particle size distributions have the widest influence on segregation, whereas variations in density are more or less insignificant, except for gas fluidization. As segregation may have a strong impact on product quality, leading for example to variations in bulk density or chemical composition, a deep understanding of this phenomenon is of great importance. [29]

Several *mechanisms of segregation* are known [29]:

1. Trajectory segregation
2. Percolation of fine particles
3. Rise of coarse particles on vibration
4. Elutriation segregation

### **Stresses in Bulk Solids**

Related to Newtonian fluids and Hooke's law, respectively, describing fluid and solid behavior, bulk solids can be classified in between these two states of aggregation. Granular materials show distinct behavior and properties whether it is moving or under static conditions, namely [37]:

- transmit no or little tensile stresses;
- transmit compression- and shear stresses under static conditions;
- begin to flow by exposure to shear stresses after reaching the critical yield point;
- own a yield point that is dependent on stress conditions;
- alter its bulk density dependent on pressure and movement.

### Stress Analysis

Considering a bulk element in a container with infinite depth and the assumption of frictionless walls, one can distinguish between vertical,  $\sigma_v$ , and horizontal,  $\sigma_h$ , stresses acting on it; these normal stresses are visualized in Figure 2.5.

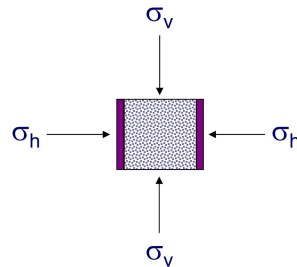


Figure 2.5.: Horizontal,  $\sigma_h$ , and vertical forces,  $\sigma_v$ , acting on a bulk element [10].

As long as the walls are assumed to be free of any frictional forces, there are no shear stresses,  $\tau$ , acting on the element. The ratio between horizontal and vertical stresses,  $\lambda$ , is a characteristic value, classifying the sample in between solid or liquid [10] and is given by

$$\lambda = \frac{\sigma_h}{\sigma_v} \quad (2.4)$$

For a Newtonian fluid <sup>1</sup> the vertical and horizontal forces would be equal, therefore  $\lambda = 1$ . However, this is not true for bulk solids, where  $0.3 < \lambda < 0.6$ , as well as for perfectly stiff solids, where  $\lambda = 0$  [10].

---

<sup>1</sup>A Newtonian fluid shows a linear relationship between stress and strain rate, with the dynamic viscosity as constant of proportionality. For example, water is a Newtonian fluid, that does not change its fluid properties upon shearing.

In the case mentioned above, where no shear stresses occur ( $\tau = 0$ ), the normal forces acting on the bulk element are extreme values and are referred to as principal stresses. Thereby, the larger principal stress is indicated as major principal stress,  $\sigma_1$ , and the smaller principal stress as minor principal stress,  $\sigma_2$ .

Considering a triangular element taken from the bulk solid element, defined by an arbitrary angle  $\alpha$  (see Figure 2.6(a)), one can apply an equilibrium of forces in order to calculate the normal and shear stresses ( $\sigma_\alpha, \tau_\alpha$ ) acting on it [35].

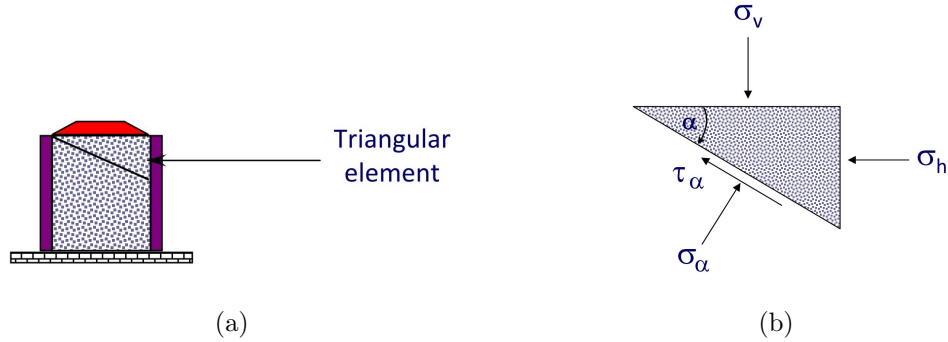


Figure 2.6.: Triangular element of bulk solid (a) and stresses acting on it (b).

The following equations allow the calculation of the normal,  $\sigma_\alpha$ , and shear stresses,  $\tau_\alpha$ , acting on a plane inclined by an arbitrary angle  $\alpha$ , derived from the equilibrium of forces acting on the bulk element [35]:

$$\sigma_\alpha = \left( \frac{\sigma_v + \sigma_h}{2} \right) + \left( \frac{\sigma_v - \sigma_h}{2} \right) \cdot \cos(2\alpha) \quad (2.5)$$

$$\tau_\alpha = \left( \frac{\sigma_v - \sigma_h}{2} \right) \cdot \sin(2\alpha) \quad (2.6)$$

### Mohr Circle

The Mohr Circle is used to describe stresses occurring in a bulk material when external stresses are applied. Basically, it illustrates all possible combinations of normal and shear stresses acting on any plane in a powder sample [29].

The Mohr Circle is constructed by plotting in a diagram the calculated values of  $\sigma_\alpha$  and  $\tau_\alpha$  for all possible values of angle  $\alpha$ . The center of the circle is always located at  $\sigma_m = \left( \frac{\sigma_v + \sigma_h}{2} \right)$  and  $\tau_m = 0$ , whereas the radius of the circle is defined by  $\sigma_m = \left( \frac{\sigma_v - \sigma_h}{2} \right)$  [35]. Figure 2.7 represents a Mohr Circle that is well defined by its principal stresses

$\sigma_1$  and  $\sigma_2$ , where  $\sigma_1$  is the major principal stress and  $\sigma_2$  the minor principal stress. For these principal stresses, the shear stresses are zero ( $\tau = 0$ ), and the effective angles of  $\alpha$  are  $\alpha = 0$  and  $\alpha = \frac{\pi}{2}$  [10].

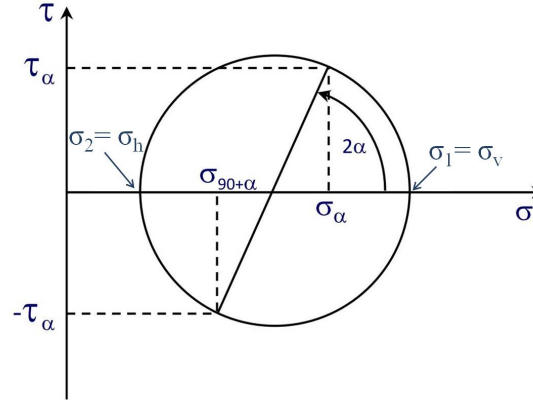


Figure 2.7.: Analysis of forces using the Mohr Circle [34].

### Analysis of Powder Properties by means of Mohr Circle Construction

In order to gain access to powder properties, a Mohr Circle can be constructed with the data obtained from shear cell measurements (see section 2.1.3.1 for details).

Therefore, the yield loci, i.e. the values for normal and shear stresses at which flow occurs, are taken from the shear cell tests and plotted in a diagram. Here, the x-axis indicates the normal stresses  $\sigma$  and the y-axis the shear stresses  $\tau$ . A best fit line is then drawn and extrapolated to the y-axis. The slope of this line is called angle of internal friction  $\varphi_i$ , while the intersection with the y-axis at  $\sigma = 0$  is called cohesion,  $\tau_0$ . For further analysis, two Mohr Circles, tangential to the yield loci are drawn [29] (see Figure 2.8).

**1. Smaller Circle.** This circle passes through the origin of the plot and is tangential to the best fit line. This circle provides the unconfined yield strength (UYS), also known as  $\sigma_y$  which is the greater value at the intercept with the x-axis and indicates the normal stresses under which powder flow occurs.

**2. Larger Circle.** The larger circle is also tangential to the best fit line and passes through the end point of the yield loci, representing conditions for critical failure. The larger value at the intercept with the x-axis represents the major principal stress

(MPS), also known as compaction or consolidation stress  $\sigma_c$ , representing the largest normal stress occurring within the powder.

As soon as powder flow occurs, the density and stresses within the bulk decrease until a steady-state motion, i.e. a point of stationary flow, is reached. This point, related to a certain bulk density, is described by the larger Mohr Circle, also referred to as End-Mohr circle. The straight line tangential to the End-Mohr circle and passing through the origin, called effective yield locus, represents the stresses and density changes during "flowing". This line is characterized by a slope which is the effective angle of internal friction,  $\varphi_e$ . [37]

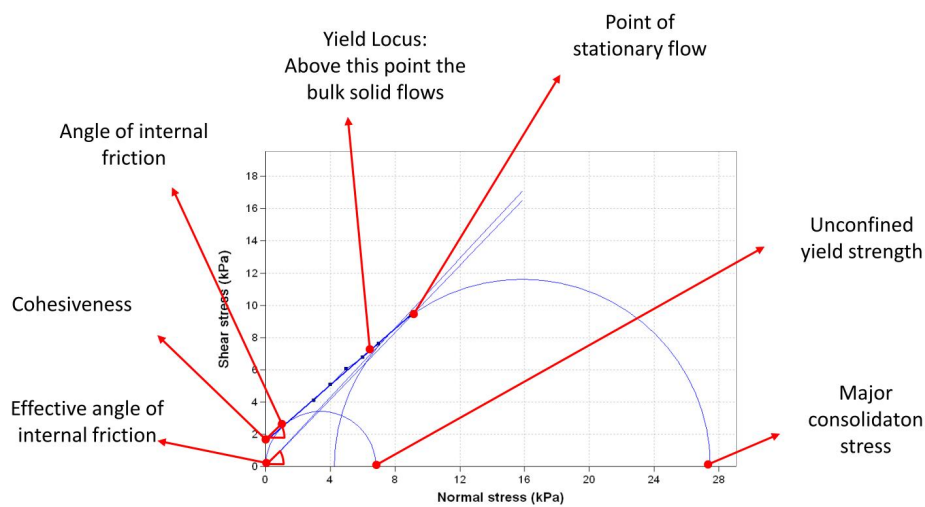


Figure 2.8.: Characteristic powder properties derived by Mohr Circle analysis [30].

### 2.1.3. Equipment Properties and Hopper Design

Considering the problems that can occur during processing solids (see section 2.1.2), it is important to have the appropriate design of hoppers, bins and feeders to avoid potential incompatibilities between powders and the equipment. These incompatibilities may result in significant process downtimes, or even compromise the quality of the product and create potential safety issues [10].

There are two important design criteria that have to be considered when constructing a hopper, namely the hopper angle and hopper outlet size. It is of great significance that the hopper angle is steep enough and the outlet size wide enough to prevent arching and to assure continuous mass flow conditions [15].

The flow pattern within a silo, whether mass flow or funnel flow occurs, is affected by the following values [37] :

- Angle of wall friction,  $\varphi_w$ ;
- Effective angle of internal friction,  $\varphi_e$ ;
- Conus angle and therefore geometry of the silo,  $\Theta$ .

Typical examples for hopper geometries, resulting in different flow behavior, are illustrated in Figure 2.9.

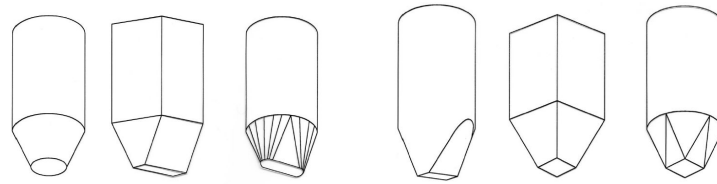


Figure 2.9.: Different styles of hoppers: conical, plane flow, transition, chisel, pyramid, square opening (from left to right) [10].

The quantities determining the flow pattern within a silo, namely the angle of wall friction, the effective angle of internal friction and the conus angle, are accessible by rheological tests.

### 2.1.3.1. Analysis of Bulk Properties by Powder Rheology

The powder rheometer is an universal powder tester (*FT4* from *Freeman Technologies*) that can measure dynamic flow, shear and bulk properties of powders and granules. Typical bulk properties to be measured are compressibility, permeability, bulk density, consolidation, wall friction and shear cell properties [10].

#### Operating Principle of the Powder Rheometer

The main part of the powder rheometer is a blade that rotates and simultaneously moves up and down through a powder sample for a defined helix angle and speed. This construction tries to generate flow conditions that closely resemble those occurring during handling and processing of powders. The parameters measured on the shaft are:

- Torque
- Axial and rotational force
- Blade height

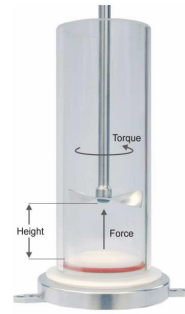


Figure 2.10.: Powder Rheometer [10].

There are many different test sequences that can be performed in order to characterize a powder. This study focused on the investigation of the bulk and material properties that are essential for designing and constructing a hopper and include the rheological tests described as follows. [10]

### Stability Test

The stability test is performed prior to the investigation of other parameters and provides information on the stability of the powder during the subsequent test cycles. A change of powder properties, e.g. breakup of particles or formation of agglomerates, would indicate low stability of the material. Similarly, cohesive or compressible powders, which can change their flow properties by getting caked or agglomerated during handling, indicate low stability as well.

During the stability test the powder is conditioned and tested alternately for seven times. The parameter measured for displaying the stability of the powder is the basic flowability energy (BFE), which is the force needed to move the blade through the powder. No change in BFE indicates stable behavior of the powder. The stability is characterized by the stability index  $SI$ , given by

$$SI = \frac{\text{energy test 7}}{\text{energy test 1}} \quad (2.7)$$

A stability index of  $SI \approx 1$  indicates a robust material, whose properties are not altered while being made to flow. A  $SI > 1$  can be the result of de-aeration, agglomeration, segregation, moisture uptake or electric charge, whereas a  $SI < 1$  can arise from e.g. attrition or de-agglomeration [10].

### Compressibility Test

The compressibility of powders represents the change of bulk density as a function of applied normal stress. This bulk property is affected by parameters like particle size distribution, cohesion, particle stiffness, particle shape and surface texture.

During this test the sample is first conditioned, while afterwards a vented piston is used to compress the powder under increasing normal stress in several steps. The normal stress is kept constant at every compression step for a fixed period of time in order to allow the sample to stabilize. The compressibility can then be calculated as a percentage change in volume before and after compression and is described by the compressibility index  $CI$  given by

$$CI = \frac{\text{density after compression}}{\text{conditioned bulk density}} \quad (2.8)$$

### Shear Cell Test

The knowledge of shear properties is important with regard to stresses acting on a bulk material and also to find out the critical yield point indicating powder flow.

During the shear cell test a shear head induces vertical and rotational stresses. As soon as the blades of the shear cell reach the powder bed, a defined normal stress  $\sigma$  is applied. Afterwards, the shear head begins to rotate inducing a shear stress  $\tau$ , while the normal stress is kept constant. If the powder bed resists the rotation, the shear stress is increased until the powder fails and the yield point is reached. Both, the shear and the normal stresses at this point are recorded and the tests sequence is repeated for several levels with decreasing normal stresses. The test can then be repeated for different ranges of normal pre-consolidation stresses (3 kPa, 6 kPa, 9 kPa, 15 kPa) to achieve a series of yield loci for better resembling real process conditions. Before each test cycle, the powder is pre-sheared in order to achieve steady-state conditions.

Comparing the absolute values of the shear stresses at different levels of normal stresses, the likeliness of a powder to flow can be estimated. The greater the value of the shear stress, the more difficult the powder will flow. Thus, steep yield loci indicate high sensitivity to increasing levels of consolidation [10].

The obtained yield locus represents the stress conditions at a defined bulk density, namely

- $\sigma$ - $\tau$ - values below the yield locus indicate stable behavior and the powder is at rest;
- $\sigma$ - $\tau$ - values above the yield locus are impossible, since the powder cannot support such stress combinations. [29, 37]

### Wall Friction

In order to assess the influence of hopper wall materials on the flow behavior of the powder, it is important to know about the frictional forces between them.

The test sequence for analyzing the wall friction angle is almost identical to that of the shear cell test. A wall friction head, containing a disc made up of the wall material, induces normal and shear stresses on the powder sample. After a defined normal stress is reached, the friction head begins to shear and the torque increases until the resistance of the powder bed is overcome and a maximum torque is reached. The shearing process of the friction head continues, so that the torque can be measured in order to provide a steady-state shear stress. More details on this test can be found in [10].

*Note: The powder samples are conditioned prior to each test in order to achieve standardized conditions of the powder packing. Conditioning is performed by a downward and upward motion of the blade through the powder bed. Thereby, precompactions or excess air is removed and a homogeneously packed powder bed is assured. [10]*

## 2.2. Dissolution

*”Dissolution is a mass transfer unit operation during which the solid particle decreases in size and ultimately disappears as it is incorporated as solute in the liquid.” [26]*

### 2.2.1. Dissolution Process

After pouring a powder on the surface of a liquid, the dissolution process of the bulk material takes place in four individual steps [24]:

1. *Wetting*: penetration of liquid into the porous system due to capillary action.
2. *Submerging* of the particles in the liquid.
3. *Dispersion* of the powder in the liquid (dispersibility).
4. *Dissolution* of the particles if soluble (solubility).

All these steps have an influence on the overall kinetics of the process.

### Wetting

Wetting and, above all, the wettability of powders and bulk materials is a crucial property in many industrial applications, like e.g. dispersion, granulation, coating, drying and dissolution [22]. Considering dissolution, wetting is the driving force for mass transfer between solids and liquids, hence the wettability of a material may strongly influence the dissolution rate [28].

The extent of wetting of a liquid on solid surfaces is determined by the contact angle  $\theta$  between the phases involved. This value is a function of the physical and chemical properties of the liquid, but also depends on the surface roughness, on sorption layers, on chemical heterogeneity and swelling, as well as on partial dissolution of the solid [22]. The contact angle is given by the Young equation

$$\cos\theta = \frac{\gamma_{SV} - \gamma_{SL}}{\gamma_{LV}} \quad (2.9)$$

where  $\gamma_{SV}$  is the interfacial tension between solid and vapor phases,  $\gamma_{SL}$  is the interfacial tension between solid and liquid phases and  $\gamma_{LV}$  is the interfacial tension between liquid and vapor phases.

Depending on the degree of wetting, different droplet shapes are observable when a fluid is placed upon a solid surface (see Figure 2.11). This shape allows to quantify the wettability of a certain material [1]:

|                                 |                      |
|---------------------------------|----------------------|
| $\theta = 0^\circ$              | perfect wetting      |
| $0^\circ < \theta < 90^\circ$   | partial wetting      |
| $90^\circ < \theta < 180^\circ$ | non wetting          |
| $\theta = 180^\circ$            | complete non wetting |

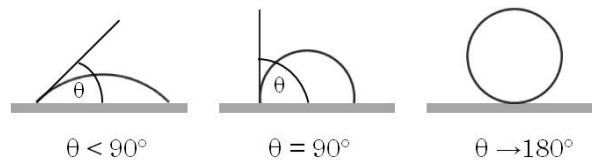


Figure 2.11.: Contact angles indicating different wettability.

If water is used as wetting liquid, the contact angle can be used to measure the degree of hydrophobicity. Therein, a solid is referred to be hydrophobic if the contact angle is greater than  $90^\circ$  [22].

### 2.2.2. Dissolution and Mass Transfer in Solid-Liquid Systems

The most important step within the dissolution process is the mass transfer from the solid to the liquid phase. Many industrial applications involve mass transfer phenomena, some examples are [26]:

- Leaching;
- Dissolution of solids with or without chemical reaction;
- Precipitation;
- Crystallization - nucleation and crystal growth;
- Adsorption;
- Desorption;
- Ion exchange;
- Solid-catalyzed reactions;
- Suspension polymerization.

#### Mass Transfer Regimes in Solid-Liquid Systems in a Stirred Vessel

Considering the dissolution process in a stirred vessel, the transfer of mass from the solid to the liquid state of matter is characterized by three rate-controlling steps [26]:

##### 1. Film Diffusion

Diffusion of the solid material in the liquid film surrounding the solid particles.

##### 2. Particle Diffusion

Diffusion within the particles: in pores or through the solid phase itself.

##### 3. Surface Reaction

Chemical reaction at the surface of the particle.

Among these steps, only the film diffusion step is influenced by stirring and agitation.

### Mass Transfer and Influencing Variables in a Stirred Vessel

As soon as a soluble solid gets in touch with a liquid phase, material is released and dissolved into the liquid surrounding the solid particle. The mass transfer occurring during this process depends on the mass transfer coefficient  $\beta$ , the solid-liquid interfacial area, being the total surface area  $A$  of the particles, and the density gradient within the liquid  $\Delta\rho$  [21]. The dissolved mass per time step  $\dot{M}$  of the particles is then given by

$$\dot{M} = A \cdot \beta \cdot \Delta\rho \quad (2.10)$$

Introducing the following relationship (Equation 2.11) for the mass transfer coefficient  $\beta$ , one can see that the mass flow  $\dot{M}$  is also a function of the **diffusion coefficient**  $D$  and the **particle diameter**  $d_p$ .

$$\beta = \frac{Sh \cdot D}{d_p} \quad (2.11)$$

The term  $Sh$  represents the Sherwood number, which can be usually described as a function of the Reynolds  $Re$  and Schmidt  $Sc$  numbers

$$Re = \frac{v \cdot d_p}{\nu} \quad (2.12) \quad Sc = \frac{\nu}{D} \quad (2.13)$$

where  $\nu$  is the **viscosity** of the solution. Many empirical correlations are available in literature to correlate the Sherwood number to  $Re$  and  $Sc$ . For example, in case of laminar flow around a sphere and for  $Re > 10^5$  and  $0.6 < Sc < 2000$ , the relation of POHLHAUSEN states

$$Sh_{lam} = 0.664 \cdot \sqrt{Re_{L'}} \cdot Sc^{1/3} \quad (2.14)$$

Other empirical and semi-empirical relations for calculating the Sherwood number are listed in Table 2.2 [3].

|                     | Re         | Sc          | Sh   |
|---------------------|------------|-------------|--|
| Garner/Suckling     | 100 – 700  | 1100–2200   | $2 + 0.95 \cdot \sqrt{Re} \cdot Sc^{\frac{1}{3}}$  |
| Frössling           | > 100      | $\leq 1000$ | $2 + 0.552 \cdot \sqrt{Re} \cdot Sc^{\frac{1}{3}}$ |
| Steinberger/Treybal | 10 – 17000 | 1 – 70000   | $2 + 0.347 \cdot Re^{0.62} \cdot Sc^{0.31}$        |
| Rowe et al.         | 25 – 1150  | 1220        | $0.79 \cdot \sqrt{Re} \cdot Sc^{\frac{1}{3}}$      |

Table 2.2.: Empirical and semi-empirical relations for calculating the Sherwood number.

The dimensionless numbers for mass transfer can be expressed as a function of physicochemical properties of solids and liquids like particle diameter, liquid density and viscosity and the free settling velocity [26]:

|  |  |   |
|--|--|---|
| Reynolds number  | Schmidt number                                   | Sherwood number                               |
| $Re = \frac{\rho_L \cdot V_t \cdot d_p}{\mu_L} \quad (2.15)$ | $Sc = \frac{\mu_L}{\rho_L \cdot D} \quad (2.16)$ | $Sh = \frac{\beta \cdot d_p}{D} \quad (2.17)$ |

In a stirred vessel, the mass transfer due to diffusion is enhanced by agitation. In fact, stirring affects the hydrodynamic environment and, in particular, the boundary layer around the particles, which is as well a function of the *physicochemical properties* of the solid-liquid system. Thus, apart from the diffusion coefficient, particle diameter, liquid density, viscosity and the relative velocity  $v_{rel}$  between the solids and the liquid have an impact on mass transfer.

The relative velocity varies dependent on the particles location within the vessel and is difficult to estimate. Thus, for practical applications, this value is regarded to be equal to the free settling velocity of the particles  $V_t$ .

Another important parameter affecting mass transfer is the *rate of renewal* of the boundary layer, which is controlled by the intensity of turbulence around the particle and the convective velocity distribution in the vessel. Hence, increasing *agitation speed* results in increasing mass transfer, if the process is mass transfer controlled. Figure 2.12 indicates the relationship between relative mass transfer and impeller power. As soon as the point of complete suspension is reached, the rate of mass transfer decelerates, indicating a bulk reaction controlled process. [26]

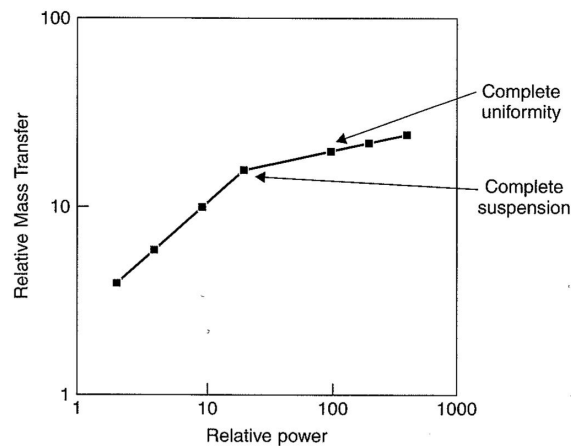


Figure 2.12.: Relative mass transfer as function of impeller power [26].

Summing up, the following statements can be made related to solid-liquid mass transfer in stirred vessels:

- As long as not all of the particle's surface area is exposed to the liquid phase, mass transfer in agitated vessels increases rapidly with increasing impeller speed. This is due to increasing surface area  $A$  of the particles and increasing mass transfer coefficient  $\beta$  up to the just suspended state, where the entire surface area is available for mass transfer. Afterwards, all the particle surface area is already exposed to the liquid and only  $\beta$  continues to increase, but to a much smaller extent, as already shown in Figure 2.12. [26]
- When stirring with a speed equal to  $N_{js}$ , which is the minimum speed required to achieve *just suspended* conditions, the mass transfer coefficient  $\beta$  is neither a function of the geometry of the vessel and impeller, nor power consumption affects the mass transfer coefficient. [7]
- $\beta$  also depends on the hydrodynamic regime within the agitated vessel: under turbulent conditions, the mass transfer coefficient is independent of the particle diameter and the density difference [7],
- at impeller speeds close to  $N_{js}$ ,  $\beta$  is strongly influenced by the density difference between the particles and the liquid. [7]

## 2.3. Mixing and Homogenization

This study only focuses on solid-liquid mixing, whose main intention is the formation of a homogeneous slurry, as well as the advancement of the dissolution process by means of accelerating the mass transport between the solid and liquid phases. The main goals of mixing are [26]:

- Suspension of solids;
- Resuspension of settled solids;
- Incorporation of floating solids;
- Dispersion of solid aggregates or control of particle size from the action of fluid shear, as well as any abrasion due to particle-particle and impeller-particle impacts;
- Mass transfer across the solid-liquid interface.

### 2.3.1. Process Parameters

Considering the dissolution process as a whole, there are many factors, apart from the bulk properties, having an influence on the fluid-solid hydrodynamics and dissolution behavior. Among others, physical properties of the fluid, process operating conditions, geometric parameters of the equipment and agitation conditions may not be ignored. A more detailed description of all parameters affecting the process is proposed by Paul et al. [26]:

1. Physical properties of the liquid
  - Liquid density
  - Density difference between solids and liquids
  - Liquid viscosity
2. Physical properties of the solid
  - Solid density
  - Particle size
  - Particle shape or sphericity
  - Wetting characteristics of the solid
  - Agglomerating tendencies of the solid
  - Hardness and friability characteristics of the solid

### 3. Process operating conditions

- Liquid depth in the vessel
- Solids concentration
- Volume fraction of solid
- Presence or absence of gas bubbles

### 4. Geometric parameters

- Vessel diameter
- Bottom head geometry
- Impeller type, geometry and diameter
- Impeller clearance from the bottom of the vessel
- Liquid coverage above the impeller
- Baffle type and geometry and number of baffles

### 5. Agitation conditions

- Impeller speed and power
- Level of suspension achieved
- Liquid flow pattern
- Distribution of turbulence intensity in the vessel

## 2.3.2. Hydrodynamics of Solid Suspension and Distribution

The energy required to suspend and mix particles comes from mechanical stirrers that induce agitation within the vessel. Thereby, complex flow fields are created that are responsible for the distribution of the particles within the liquid. The degree and quality of mixing is strongly influenced by the geometry of the impeller, which has a great impact on the hydrodynamic interactions between the particles and the liquid. The velocities of the particles generated within the flow field depend on their density compared to the density of the liquid: particles having the same density will move with the liquid, whereas heavier particles will tend to settle down. [26]

### Settling Velocity

The velocity of a solid particle settling down in a quiescent fluid is referred to as the free settling velocity. In an agitated vessel, the settling velocity is difficult to be accessed, even if it is always less than the free settling velocity [13]. Under laminar

flow conditions, where  $Re_p < 0.3$ , the free settling velocity  $V_t$  is given by

$$V_t = \frac{g \cdot d_p^2 \cdot (\rho_S - \rho_L)}{18 \cdot \mu} \quad (2.18)$$

where  $d_p$  is the particle diameter,  $g$  the acceleration due to gravity,  $\rho_S$  and  $\rho_L$  the solid and liquid densities, respectively and  $\mu$  the dynamic viscosity of the liquid. [26]

For turbulent flow behavior, where  $1000 < Re_p < 35 \cdot 10^4$ , the free settling velocity can be calculated according to

$$V_t = 1.73 \cdot \left( \frac{g \cdot d_p \cdot (\rho_S - \rho_L)}{\rho_L} \right)^{1/2} \quad (2.19)$$

Therein,  $Re_p$  designates the particle Reynolds number.

The settling velocity of the bulk material is influenced by different parameters [26]:

### 1. Effect of Solids Particle Size and Distribution

The settling velocity of a particle is proportional to its size, implying faster settling velocity for larger particles. For practical applications, it is recommendable to take account of the largest particle size for any process relevant calculations.

### 2. Effect of Particle Shape and Orientation to Flow

The settling velocity of a particle also depends on its shape, which is usually expressed as sphericity. The sphericity is referred to as the ratio of the surface area of a spherical particle of the same volume to that of a non spherical particle. Equations 2.18 and 2.19 are only valid for particles with a sphericity between 0.7 and 1. For particles having a sphericity less than 0.7, the influence of shape on the settling velocity has to be investigated experimentally.

### 3. Effect of Solid Concentration

Considering a vast number of particles being suspended, the free settling velocity decreases by increasing the number of particles in the vessel. Here, *hindered settling* is observable due to various reasons [26]:

- Interaction with neighboring particles;
- Interaction with the fluid moving upwards due to downward motion of the particles;
- Increase of viscosity and density of the solution.

### States of Solid Suspension and Distribution

Considering the degree of suspension within a stirred vessel, three different regimes are observable [26] (see Figure 2.14):

#### 1. On-Bottom Motion or Partial Distribution

The characteristic indicator for this regime is the presence of particles at the bottom of the vessel. This leads to insufficient mass transfer, as a vast number of particles settles on the bottom and not the entire surface of the particles is accessible for any kind of interactions.

#### 2. Off-Bottom or Complete Suspension

This state of suspension is indicated by a complete suspension of the particles. There are no particles settled down and the entire particle surface is available for mass or heat transfer, or any other chemical reaction. According to these *just suspended* conditions, a minimum agitation speed  $N_{js}$  is necessary to obtain off-bottom suspension.

#### 3. Uniform Suspension

Uniform suspension refers to the conditions under which the particle concentration and particle size distribution is uniform throughout the vessel. A change of impeller speed does not alter the solids distribution within this regime. The state of uniform suspension is the goal of many process operations, as homogeneous suspensions are desired for most applications.

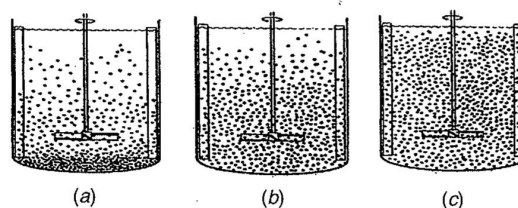


Figure 2.13.: States of solid suspensions: (a) partial (b) complete (c) uniform.

The transition from partial to uniform suspension needs the input of energy. The amount of energy depends on the settling velocity of the particles: particles with high settling velocities require greater energy inputs than slowly settling particles.

### 2.3.3. Selection and Design Issues for Solid-Liquid Equipment

In order to design a mechanical stirred mixing system, three main parts of equipment have to be considered:

- Tank;
- Baffles;
- Impeller.

#### Tank and Number of Impellers

The size and shape of the tank depends on the process needs and the mode of process operations: batch, semi-batch or continuous. Ideally, the geometry of the tank should fulfill the requirements for a wide range of filling levels [16].

The design of the vessel, in particular the geometry of the bottom head, strongly influences the flow pattern and mixing behavior within the tank. Dished bottom heads should be favored in order to achieve complete suspensions, as they require 10 to 20 % lower impeller speeds. [23, 26]

Another important design criterion is the ratio of liquid depth  $H$  to vessel diameter  $T$  (see Figure 2.14). This value determines the number of impellers required to assure uniform suspension. If the distance from the impeller to the bottom or the vessel walls is too high, a homogeneous distribution of the particles is not assured. Hence, the following design tips should be taken into account for choosing the appropriate number of impellers [26]:

- A single impeller for  $H/T < 1.3$  assuring off-bottom suspension
- Dual impellers for  $1.3 < H/T < 2.5$  assuring uniform suspension of fast-settling solids
- Vessels with a ratio  $2.5 < H/T$  are a poor choice for solid suspension

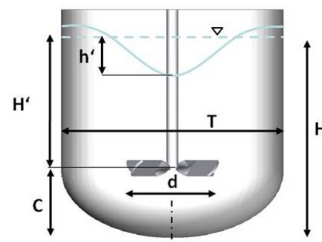


Figure 2.14.: Characteristic dimensions of a stirred tank with dished bottom head [16].

### Baffles

Baffles have the ability to advance and improve the mixing behavior within the vessel. They make sure that the particles experience an up- and downward motion instead of being subjected to swirling flow. This is in particular true for particles having a greater density than the fluid. The following design issues are recommended for choosing the appropriate baffles (see Figure 2.15) [26]:

- Using steel or alloy vessels, it is recommended to utilize four flat-blade baffles which should extend to the lower edge of the lower impeller;
- For glass-lined tanks the usage of a minimum of two fin type baffles is proposed. Nevertheless, these types of baffles are less effective than the standard four flat-blade baffles;
- Considering the position and orientation of the baffles, the edge of the fin must point toward the vessel wall and the flat face perpendicular to the tangential flow.

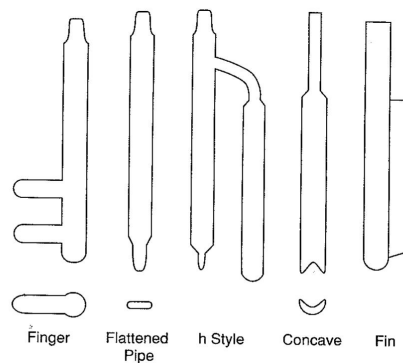


Figure 2.15.: Common glass-lined baffle types [26].

## Impeller

The choice of the appropriate impeller is of great importance and depends on the process requirements, as well as on the knowledge of the physical fluid properties. There is a great number of impeller types used for industrial applications, but in general one distinguishes between turbines and close-clearance impellers, as shown in Figure 2.16.

Turbine impellers are used for mixing fluids of low to medium viscosity and can be divided according to their flow pattern, being axial or radial (see Figure 2.17). High viscosity fluids require close-clearance impellers which are larger, having almost the size of the tank, in order to assure mixing at the macro-scale.

Considering solids suspensions, the use of small pitched blade impellers with a diameter  $d < T/2.5$ , located close to the bottom of the vessel ( $C < T/4$ ), are advantageous. Discharging of the solids during slurry transfer is also supported by this type of impeller. The impeller to tank bottom clearance  $C$  is crucial for the design of an impeller, as a clearance of  $C = T/4$  is recommended for hydrofoil type impellers (see Figure 2.16(a)), while a value of  $C = T/3$  for pitched blade turbines (see Figure 2.17(a)).

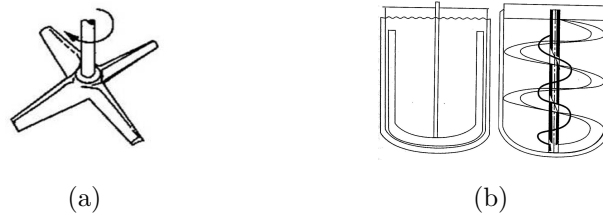


Figure 2.16.: (a) Hydrofoil turbine impeller and (b) close-clearance impellers: anchor (left) and helical ribbon (right) [26].



Figure 2.17.: (a) Axial flow impeller: pitched blade turbine and (b) radial flow impeller: open flat blade [26].

### Impeller Speed

The minimum impeller speed  $N_{js}$  required for *just suspended* conditions, can be calculated according to Zwietering by [12]

$$N_{js} = S \cdot \nu^{0.1} \cdot \left( \frac{g \cdot (\rho_S - \rho_L)}{\rho_L} \right)^{0.45} \cdot X^{0.13} \cdot d_p^{0.2} \cdot d^{-0.85} \quad (2.20)$$

where  $S$  is a dimensionless particle suspension parameter, depending on the impeller type and the  $d/T$  ratio,  $\nu$  is the kinematic viscosity of the liquid,  $g$  the acceleration due to gravity,  $\rho$  the densities of the solid  $S$  and the liquid  $L$ ,  $d_p$  the particle diameter,  $X$  the initial solids mass fraction and  $d$  the diameter of the impeller. Representative values of  $S$  can be found in literature for a variety of impellers [26].

As can be seen from Equation 2.20,  $N_{js}$  is not strongly influenced by fluid and particle properties like viscosity and particle diameter, what is indicated by small exponents. In contrast, the density difference has a greater impact on the minimum agitation speed. During progression of the dissolution process,  $N_{js}$  will decrease as the concentration of the liquid increases.

Nevertheless, the actual impeller speed has to be identified experimentally, but will always be higher than the minimum speed  $N_{js}$ . [26]

## 3. Experimental Procedure

In this section, the object of investigation was a model system of granular PEG and PEG dissolved in water, respectively. The main focus was turned on the characterization of the powder and bulk properties, on the analysis of the dissolution behavior, as well as on the assessment of the solution attributes. For measuring the dissolution kinetics, a lab-scale tank was set up and the change in concentration was followed using MIR-spectroscopy techniques. In addition, the influence of particle size and impeller speed on the dissolution behavior was evaluated.

### 3.1. Design of Experiment

The main goal of the experimental investigations was the analysis of the bulk and particle properties, the solution attributes and the dissolution behavior as a function of particle size.

Considering the dissolution process, it was important to assess and characterize the parameters having an influence on the mass transfer between solids and liquids, namely:

- Particle size;
- Viscosity of the PEG solutions;
- Density of the PEG solutions;
- Impeller speed.

Two of them, particle size and impeller speed, were varied during the experiments. To obtain different particle sizes, PEG was milled in a ball mill under varying conditions, namely the filling capacity of the milling vessels and the grinding duration. Afterwards, the PSD was measured and two lots with distinct PSD were chosen for further analysis.

These two lots, namely Lot 3 and Lot 10, were used to determine and compare the following parameters <sup>1</sup>:

- Particle shape;
- Specific surface area of the particles;
- Rheological behavior;
- Dissolution behavior in a stirred tank.

Hence, the dissolution experiments were carried out with two lots of PEG, representing distinct particle size, and two different impeller speeds each, namely 90 and 150 rpm. The PEG bulk was fed in a defined number of steps (Table 3.1) and the amount of PEG per step was equal to 60 g for all cases. After the bulk material of step 1 was completely dissolved, another 60 g were fed to the tank until a homogeneous solution was reached; this was repeated for several steps.

| Lot      | Impeller speed<br>[rpm] | Number of<br>steps |
|----------|-------------------------|--------------------|
| 3 and 10 | 90                      | 4                  |
| 3 and 10 | 150                     | 5                  |

Table 3.1.: Parameters for the dissolution experiments.

To assess the solution attributes of PEG dissolved in water, standard solutions with increasing concentration of PEG were prepared and the densities and viscosities were measured. Additionally, the saturation concentration, a parameter crucial for mass transfer calculations, was determined.

## 3.2. Analysis of Bulk and Particle Properties

The material used for all experiments was polyethylene glycol 6000, which consists of solid, white platelet-shaped particles. The samples were taken from a plastic bag and directly used for further experiments.

<sup>1</sup>Particle shape and surface area were also determined for Lot native, being native PEG without any pre-treatment.

### Sample Description

The labels used for identification of the samples throughout all experiments can be found in Table 3.2. The term *batch* refers to one charge of the milling vessel. Since several hundred grams of PEG were required for the experiments, the material was milled in several batches at 60 g each. Details on the samples and the milling parameters for the different lots can be seen in section 3.2.1.

| Label      | Sample description                                       |
|------------|--|
| Lot native | Native PEG 6000 without any pre-treatment                |
| Lot 3      | PEG milled for 3 min                                     |
| Lot 5      | PEG milled for 5 min                                     |
| Lot 7      | PEG milled for 7 min                                     |
| Lot 10     | PEG milled for 10 min                                    |
| Batch 1-5  | various batches of PEG, milled for 3 min and 10 min each |

Table 3.2.: Sample labeling.

#### 3.2.1. Variation of Particle Size by Milling

In order to get particles with different sizes, the PEG powder was milled in a *Retsch* ball mill under varying conditions and settings. The variable parameters chosen for the milling experiments were the *filling capacity* of the milling vessels and the *grinding duration*. The rotation frequency for all milling experiments was set to 60 %, which corresponds to 60 % of the maximum capacity of the ball mill.

The ball mill consists of two cylindrical vessels made of agate stone which rotate under controlled conditions. Each of them contains eight balls, which were loaded before the sample was added. This led to a better distribution of the balls and the granular material. Additionally, under these conditions the samples were not compacted that much and the balls could move upwards during milling. For this reason, all further experiments were carried out using this adjustment, namely balls being arranged on bottom of the vessel.

### Influence of Filling Capacity on the PSD

In order to investigate the influence of the filling capacity of the milling vessels on the particle size distribution, the vessels were filled with varying amounts of PEG and milled for 5 minutes each. The grinding duration and the frequency of the ball mill were kept constant for all samples. The settings for these experiments can be found in Table 3.3.

| Sample Nr. | Filling Capacity [g] | Frequency [%] | Grinding Time [min] |
|------------|----------------------|---------------|---------------------|
| KM 2       | 30                   | 60            | 5                   |
| KM 1       | 60                   | 60            | 5                   |
| KM 3       | 70                   | 60            | 5                   |
| KM 4       | 90                   | 60            | 5                   |

Table 3.3.: Parameter study for the ball mill - variations in filling capacity.

### Influence of Grinding Duration on the PSD

In order to assess the variation in particle size distribution due to varying exposure time to the ball mill, samples of the bulk material were milled for 3, 5, 7 and 10 minutes each. In addition, the experiment was performed for two different filling quantities of the milling vessels, namely 60 g and 90 g. The parameters chosen can be found in Table 3.4.

| Sample Nr. | Filling Capacity [g]<br>Vessel 1/2 | Frequency [%] | Grinding Time [min] |
|------------|------------------------------------|---------------|---------------------|
| KM 8       | 60/90                              | 60            | 3                   |
| KM 5       | 60/90                              | 60            | 5                   |
| KM 12      | 60/90                              | 60            | 7                   |
| KM 10      | 60/90                              | 60            | 10                  |

Table 3.4.: Parameter study for the ball mill - variation in grinding time.

After milling, the powder samples were stored in plastic flasks, screwed down and blended in a *Turbula Typ T2F* mixer for 2 minutes at 50 rpm to achieve homogeneous blends. Afterwards, the particle size distributions were measured using image analysis.

### 3.2.2. Particle Shape

The shape analysis of the PEG particles from different lots was performed by means of microscopy as well as dynamic image analysis.

#### Microscopy

The microscopy recordings were performed on a *Leica DM4000* microscope. Prior to sampling, the plastic flasks containing the PEG samples were shaken and stirred with a spatula. Afterwards, a few milligrams were placed on the object holder and the recordings were taken.

#### Dynamic Image Analysis

The shape of the particles was determined by dynamic image analysis using the *QicPic Analysis System* by *Sympatec*. Thereby, images are recorded by a high speed camera taking 450 frames per second. At the same time, a dispersion unit fluidizes the particles to avoid overlap and moves them through the image plane [39].

### 3.2.3. Particle Size Distribution

The particle size distributions were measured on a *QicPic particle size analyzer*, based on image analysis, using the *OASIS/L* disperser and the *VIBRI/L* feeding device. The appropriate settings for analyzing the PEG powder were identified in former experiments and can be found in Table A.1.

*Sampling procedure:* the samples used for analysis were taken from the ball mill experiments. As mentioned above, the powders were stored in plastic flasks and homogenized on the *Turbula Typ T2F* mixer for 2 minutes at 50 rpm. Samples were drawn with a spoon and directly added to the chute. Each sample was measured three times and the mean values were calculated.

The dimensions used for data interpretation were the particle sizes  $x_Q$  for given Q-values (10 %, 50 %, 90 %). The Q-values are the amount of particles, in percentage of the total quantity, that are finer than a characteristic particle size,  $x_Q$ .

*Characteristic particle sizes for given Q-values:*

$x_{10}$  - 10 % of the total quantity of the particles  $< x_{10}$

$x_{50}$  - 50 % of the total quantity of the particles  $< x_{50}$

$x_{90}$  - 90 % of the total quantity of the particles  $< x_{90}$

These values were based on a  $Q_0$ -cumulative number distribution calculated by the software program *Windox*. The diameter used for size analysis was the EQPC-diameter (Figure 3.1), which corresponds to the diameter of a circle that has the same area as the projection area of the particle [39].

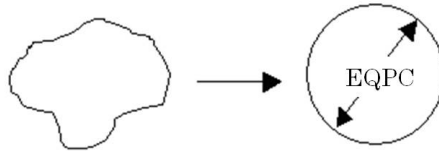


Figure 3.1.: Diameter of a circle of equal projection area.

### 3.2.4. Particle Surface Area

The specific surface area, the pore volume and the pore diameter of the bulk material were determined using nitrogen adsorption method on a *Micromeritics ASAP 2010*. This method assumes the admission of gas molecules to the clean surface of the sample under increasing pressure. This increase of gas pressure leads to an increasing number of molecules attached to the sample surface. The process continues until it is statistically reasonable to consider a monolayer of molecules to have formed on the surface. The surface area is then calculated from the number and dimensions of gas molecules adsorbed.

To remove any moisture or atmospheric vapors, the sample is first heated and purged with helium, which is a non-adsorbing gas. Afterwards, the temperature of the sample is adjusted to that of liquid nitrogen and the gas is admitted stepwise to the sample. In order to describe this process, an adsorption isotherm is established. This represents

the change of gas volume, taken up or released from the sample surface, as a function of gas pressure at constant temperature [42]. For data evaluation, the BET-model according to Brunauer, Emmett and Teller was used [4].

*Sampling procedure:* the samples were homogenized on the *Turbula Typ T2F* mixer for 2 minutes at 50 rpm, transferred to the analysis tubes, degased at 30°C and analyzed. The measurement was carried out with 3 different samples of Lot 3, Lot 10 (both from Batch 1) and Lot native and the resulting values were averaged.

### 3.2.5. Powder Rheology

For characterizing the powder bulk properties of the granular material, measurements were performed using the *FT4 Powder Rheometer* by *Freeman Technology*. All tests were carried out using a 50 mm x 85 ml split vessel.

Three different test sequences were run and, prior to any other test, a *stability test* was performed. This assured that the powder properties did not change during subsequent tests.

The *shear cell test* was performed for three different ranges of normal stresses, namely 3 kPa, 6 kPa and 9 kPa. The powder sample was the same for all tests.

The analyses of *compressibility* and *wall friction* were made afterwards, using fresh, untreated bulk material. The compressibility test was performed in 8 compression steps, starting at 0.5 kPa and increasing the normal stress up to 15 kPa.

The wall friction was determined using a 316 stainless steel disk with a surface roughness of 0.28  $\mu\text{m}$ .

All tests were performed twice and stretched over several days. Hence, there were little variations observable in the environmental conditions, such as air temperature and relative humidity. As the samples were not conditioned to same moisture content, this may slightly influences the test results.

## 3.3. Dissolution Experiments

### 3.3.1. Dissolution in a Lab-Scale Tank

In order to investigate the dissolution behavior and kinetics of PEG particles in water, a lab-scale plant was implemented. It consisted of different units, namely:

- The "reactor", a 1000 mL beaker with a diameter of 110 mm;
- A four-bladed impeller for stirring and mixing;
- A temperature control governed by a heating plate and a coupled thermostat;
- A vibrational conveyor for feeding the material with a constant feeding rate.

For evaluating the time-dependent change in concentration of the PEG-solutions, a MIR-probe was connected to the system. The dissolution experiments were performed for two different lots of PEG, Lot 3 and Lot 10, representing different particle size distributions. In addition, the influence of varying impeller speed on the dissolution behavior was evaluated. Figure 3.2 displays the installation and build-up of the lab-scale plant.

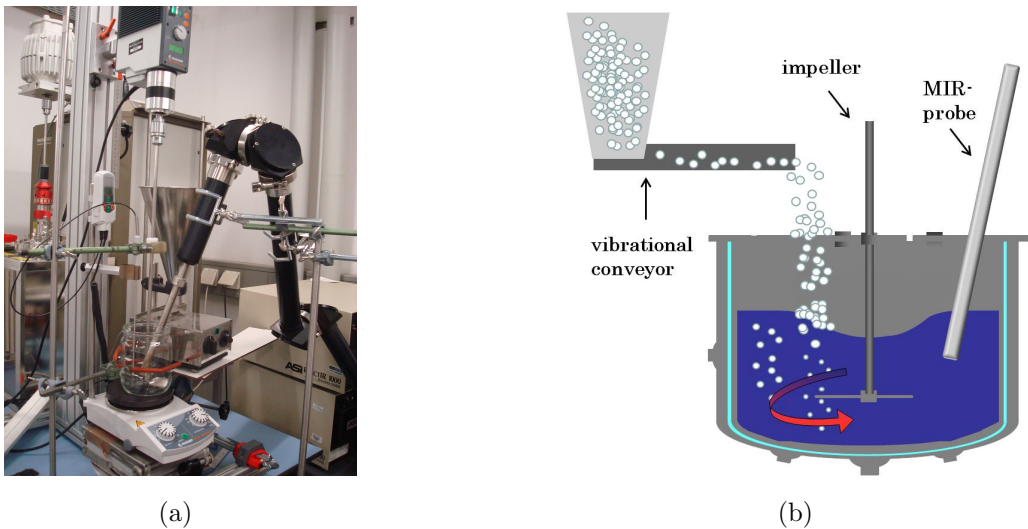


Figure 3.2.: Lab-scale plant (a) and schematic description (b).

### The Spectroscopy System

The spectroscopy system used for analysis was a *ReactIR 1000* by *ASI/Mettler Toledo* consisting of an optics module, an electronic module and a computer workstation. The SIM (**S**ample **I**nterface **M**odule) contains the detector and its optics, while the ATR (**A**ttenuated **T**otal **R**eflection) multiple reflection unit of the probe is a 0.25 mm thick diamond element [40]. The settings were chosen as follows: the resolution was set to  $8\text{ cm}^{-1}$  and the number of scans was adjusted to 64, implying that 64 interferograms per minute were recorded and co-added to produce a spectrum.

### Calibration of the MIR-System

In order to evaluate the spectral data obtained from the MIR measurements, a calibration of the spectroscopic system was performed. For this purpose, calibration solutions of 1 wt.%, 3 wt.%, 5 wt.%, 10 wt.%, 20 wt.%, 30 wt.%, 40 wt.% and 50 wt.% of PEG in deionized water were prepared. The solutions were stirred at room temperature using a magnetic stir bar for at least 5 hours to assure completely homogeneous solutions. Afterwards, the spectra of the calibration solutions were collected in order of ascending concentration.

For this purpose, the samples were filled into a 1000 mL beaker and stirred at 150 rpm. The temperature was kept constant at  $25^{\circ}\text{C}$  using a heating plate and a coupled thermostat. For each solution, 10 spectra were collected with a frequency of one spectrum per minute. After each measurement, the beaker was discharged, while the probe and the impeller were cleaned with deionized water and dried afterwards. The calibration procedure was repeated once using the same calibration solutions.

### Experimental Procedure

In order to determine and compare the dissolution behavior of the bulk material as a function of increasing concentration, thus increasing viscosity of the solution, a defined amount of PEG bulk was fed into the beaker at a feeding rate of  $170 \pm 30\text{ g/min}$ . The material was fed in a defined number of steps, e.g. 4 and 5, depending on the set of experiments. The amount of PEG fed per step was for all cases equal to 60 g.

At the beginning, the beaker was filled with 300 ml of deionized water as solvent and the temperature was kept constant at  $25^{\circ}\text{C}$ . In order to assure complete dissolution of the bulk material, the mixtures were stirred for at least 20 minutes; this minimal duration of mixing was identified in former experiments. After a homogeneous solution had been reached, 60 g of PEG were added to the solution in a next step.

### Data Evaluation

For evaluating the spectral data, the software *MATLAB* was used.

The following method was applied:

- The background spectrum of water was subtracted from every spectrum;
- A characteristic peak region of PEG, namely  $1200 - 900 \text{ cm}^{-1}$ , was chosen ;
- A base line drawn;
- The peak area was calculated (see Figure 3.3).

The same procedure was performed in order to evaluate the spectral data from the calibration experiment. Based on the calibration solutions, a regression line was plotted and used for further calculations of the concentration of the PEG solutions.

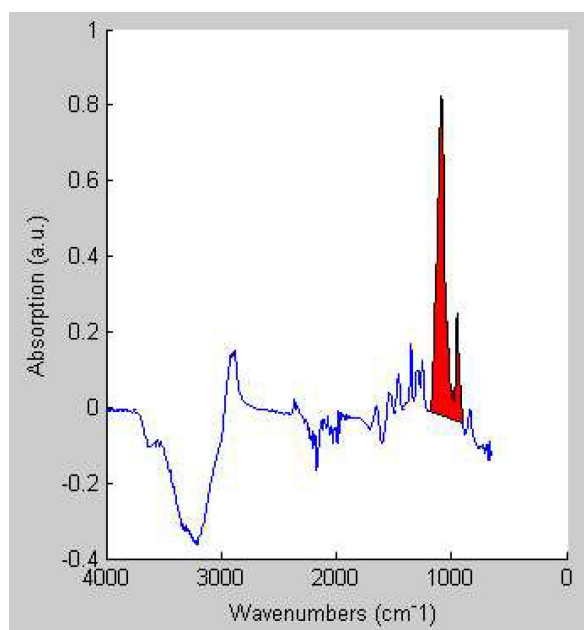


Figure 3.3.: Peak area used for evaluation of spectral data.

## 3.4. Analysis of Solution Properties

In order to gain insight into the physical properties of PEG in water, experiments on different solutions were carried out. The required amount of PEG was dissolved in deionized water and stirred well to assure homogeneous mixtures. Afterwards, the solutions were analyzed in terms of viscosity and density.

### 3.4.1. Density

The analysis of the density of the standard solutions was carried out together with the analysis of the dynamic viscosity on a *Anton Paar Stabinger Viscometer SVM 3000* at 20°C. After assuring that the standard solutions were free from bubbles, the samples were measured twice and the mean values were calculated.

### 3.4.2. Viscosity

The analysis of the dynamic viscosity was performed on a *Anton Paar Stabinger Viscometer SVM 3000* at 20°C. As well as for the analysis of the density, the measurements were repeated and the mean values calculated.

### 3.4.3. Saturation Concentration

In order to determine the saturation concentration<sup>2</sup> of PEG in water, different amounts of bulk material were dissolved in deionized water under controlled conditions and the progress of dissolution was monitored visually. For each sample, 25 ml of deionized water were filled in a 100 ml Erlenmeyer flask, tempered to  $25 \pm 2^\circ\text{C}$  using a heating plate and a coupled thermostat, then sealed using *Parafilm*. Afterwards, a defined amount of PEG was added stepwise to the flask and the mixtures were stirred over night to assure homogeneous solutions. As soon as the solutions turned out to be turbid, they were considered to be saturated.

---

<sup>2</sup>The saturation concentration of a substance in a solvent at a defined temperature corresponds to the concentration that is at equilibrium with undissolved bulk material [1].

# 4. Results and Discussion

## 4.1. Analysis of Powder Properties

The material used for all experiments was polyethylene glycol (PEG) 6000. The samples were taken from a plastic bag and directly used for further experiments.

### 4.1.1. Milling of the Particles and PSD

In order to get particles of varying fineness and size, the PEG powder was milled in a *Retsch* ball mill under varying conditions and settings, see Tables 3.3 and 3.4. Afterwards, the particle size distributions were determined by image analysis.

#### Polydispersity of the Samples

In order to characterize the polydispersity of the powder samples, meaning the width of the particle size distribution, the *span* was calculated according to

$$span = \frac{x_{90} - x_{10}}{x_{50}} \quad (4.1)$$

A narrow particle size distribution is characterized by a small span, whereas a high span indicates broad polydispersity [6].

#### Influence of Filling Capacity on the PSD

The filling capacity of the milling vessels directly influenced the final particle size, as the smallest particles were obtained for a medium filling capacity of 60 g and 70 g, respectively. Very low, 30 g, but also very high, 90 g, fill levels resulted in larger particles (see Table 4.1 for details). Hence, the filling capacity of the milling vessels could not have been neglected in preparing the particle size distribution.

| Filling Capacity [g] | $x_{10}$ [ $\mu\text{m}$ ] | $x_{50}$ [ $\mu\text{m}$ ] | $x_{90}$ [ $\mu\text{m}$ ] | Span |
|----------------------|----------------------------|----------------------------|----------------------------|------|
| 30                   | 24.5                       | 83.3                       | 216.5                      | 2.30 |
| 60                   | $22.5 \pm 0.1$             | $53.4 \pm 2.2$             | $157.8 \pm 1.5$            | 2.53 |
| 70                   | $22.8 \pm 0.2$             | $58.9 \pm 4.3$             | $178.4 \pm 23.1$           | 2.64 |
| 90                   | $23.2 \pm 0.1$             | $65.1 \pm 5.2$             | $183.9 \pm 5.0$            | 2.47 |

Table 4.1.: Influence of filling capacity of the milling vessels on PSD.

*Comment: No standard deviation for the sample of 30 g filling capacity was calculated, since it was analyzed just once.*

### Influence of Grinding Duration on the PSD

As expected, an increase of grinding duration strongly affected the final particle size distribution. Looking at the  $x_{50}$  values of the milling experiments with respect to grinding duration, one can recognize a sharp decrease in particle size with increasing exposure time to the ball mill. In addition, the span decreased while increasing grinding duration, leading to less polydispersity.

Besides, lower filling capacity of the vessels led to smaller particles, whose size also decreased with increasing grinding duration (see Tables 4.2 and 4.3). This suggested that the operating range of the ball mill was limited to a certain fill level.

| Grinding duration [min] | $x_{10}$ [ $\mu\text{m}$ ] | $x_{50}$ [ $\mu\text{m}$ ] | $x_{90}$ [ $\mu\text{m}$ ] | Span |
|-------------------------|----------------------------|----------------------------|----------------------------|------|
| 3                       | $23.0 \pm 0.3$             | $61.5 \pm 4.5$             | $186.1 \pm 10.3$           | 2.65 |
| 5                       | $22.5 \pm 0.1$             | $53.4 \pm 2.2$             | $157.8 \pm 1.5$            | 2.53 |
| 7                       | $22.4 \pm 0.1$             | $52.1 \pm 1.3$             | $144.4 \pm 5.0$            | 2.34 |
| 10                      | $22.2 \pm 0.0$             | $48.9 \pm 0.7$             | $136.2 \pm 3.0$            | 2.33 |

Table 4.2.: Influence of grinding duration on PSD; filling capacity of 60 g.

| Grinding duration [min] | $x_{10}$ [ $\mu m$ ] | $x_{50}$ [ $\mu m$ ] | $x_{90}$ [ $\mu m$ ] | Span |
|-------------------------|----------------------|----------------------|----------------------|------|
| 3                       | $23.2 \pm 0.5$       | $67.5 \pm 11.1$      | $202.7 \pm 23.8$     | 2.66 |
| 5                       | $23.2 \pm 0.3$       | $64.2 \pm 4.5$       | $189.2 \pm 13.8$     | 2.59 |
| 7                       | $23.0 \pm 0.2$       | $61.5 \pm 3.0$       | $173.4 \pm 13.5$     | 2.45 |
| 10                      | $22.7 \pm 0.1$       | $56.6 \pm 2.1$       | $170.3 \pm 14.7$     | 2.61 |

Table 4.3.: Influence of grinding duration on PSD; filling capacity of 90 g.

### Variation in PSD Between Different Batches

In order to evaluate the variation in PSD between different batches of PEG, milled under equal conditions, 5 batches were chosen and compared. The filling capacity of the ball mill was 60 g, the frequency was set to 60 % for all batches and the balls were arranged on bottom of the milling vessels.

The averaged median values  $x_{50}$  were  $63.8 \mu m$  for Lot 3 and  $50.6 \mu m$  for Lot 10, thus differed for about  $14 \mu m$  (see Table 4.4 and Figure 4.1). Lot 3 showed a larger standard deviation; this is apparent, since shorter grinding duration leads to higher polydispersity which was also confirmed by the increased span compared to Lot 10. In addition, the influence of sampling was more significant for particles with wider particle size distribution, leading to higher variations in PSD.

| Sample name         | Grinding duration [min] | $x_{50}$ [ $\mu m$ ] | Span |
|---------------------|-------------------------|----------------------|------|
| Lot 3, Batches 1-5  | 3                       | $63.8 \pm 5.4$       | 2.47 |
| Lot 10, Batches 1-5 | 10                      | $50.6 \pm 1.7$       | 2.41 |

Table 4.4.: Variations in particle size between 5 different batches of PEG milled for 3 and 10 minutes each.

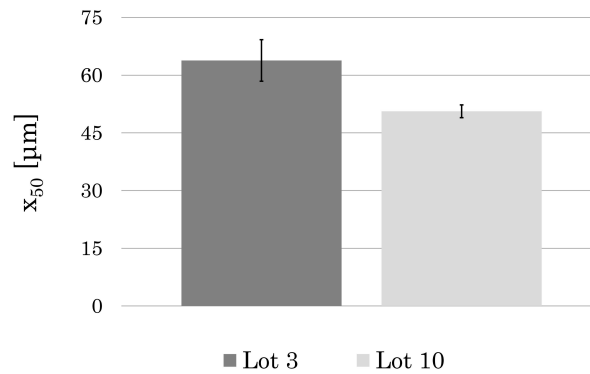


Figure 4.1.: Variations in particle size between 5 different batches of PEG milled for 3 and 10 minutes each.

### 4.1.2. Shape Analysis

The shape analysis of the PEG particles with distinct particle size was performed by means of microscopy as well as dynamic image analysis.

#### Microscopy

In general, the particle size fluctuated consistently for each sample. Therefore, the photographs were not representative for the whole particle size distribution (see Figures 4.2, 4.3, 4.4, 4.5, 4.6). Nevertheless, the recordings presented the geometrical structure of the PEG particles, namely plane, elongated platelets. This shape changed by decreasing the particle size, as the elongated structure converted to more and more squarish forms. Additionally, an increase in grinding time not only led to smaller particle size but also to an increased fraction of very fine particles.

The scale can be seen on the upper edges of the pictures and corresponds to 500  $\mu\text{m}$  each.

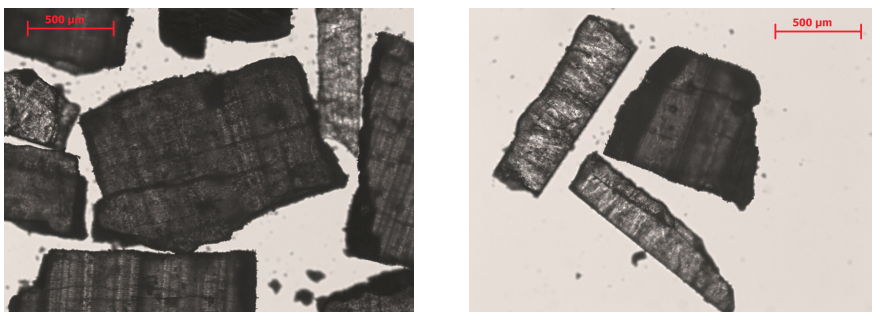


Figure 4.2.: PEG unground.

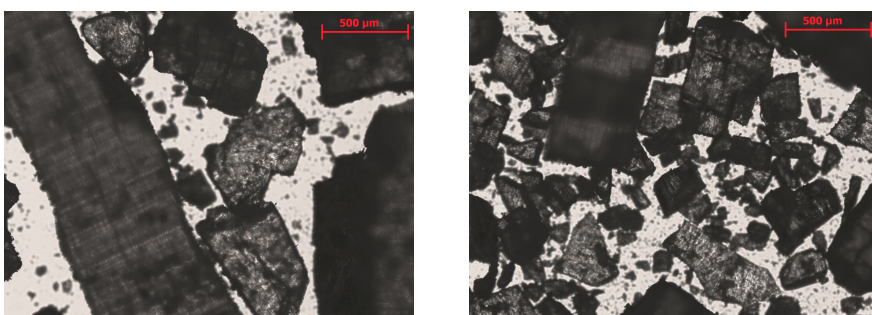


Figure 4.3.: PEG ground for 3 minutes.

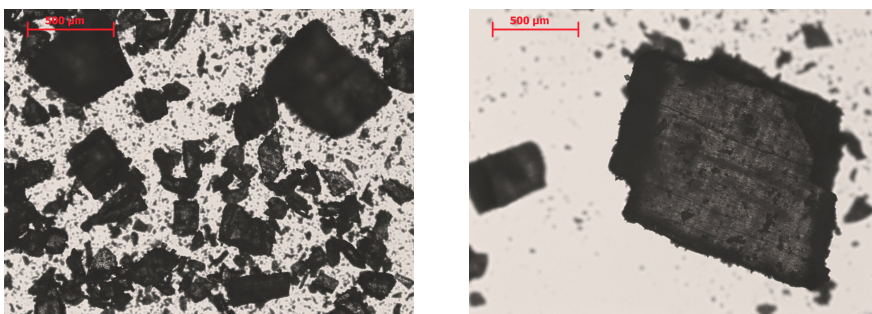


Figure 4.4.: PEG ground for 5 minutes.

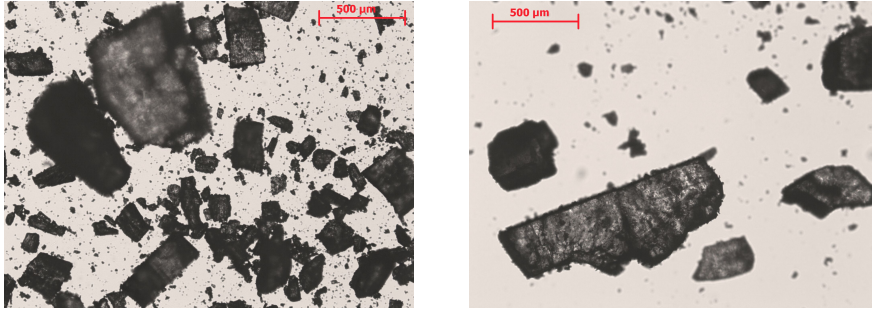


Figure 4.5.: PEG ground for 7 minutes.

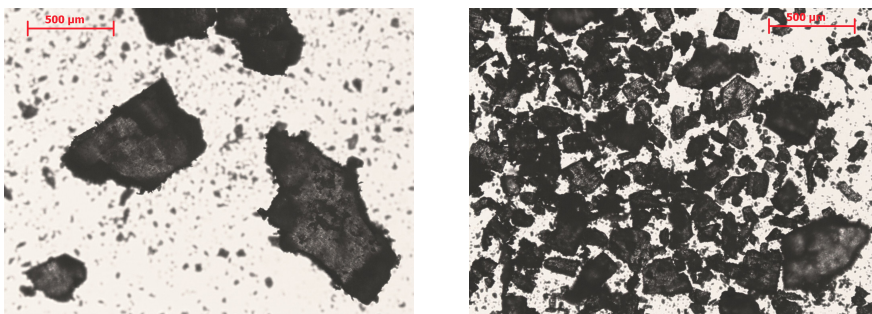


Figure 4.6.: PEG ground for 10 minutes.

### Dynamic Image Analysis

The same particle shape already observed by microscopy recordings was also analyzed by dynamic image analysis. Also in this case the elongated particles got more squarish by increasing the grinding time (see Figures 4.7, 4.8). In addition, a wide particle size distribution with a significant fraction of smaller particles could be detected as well. Like already mentioned, the particle size fluctuated in time. Thus, the images were not representative for displaying the whole particle size distribution, as they were randomly taken from the particle gallery. Nevertheless, one can see the tendency to smaller particle size with increasing grinding time.

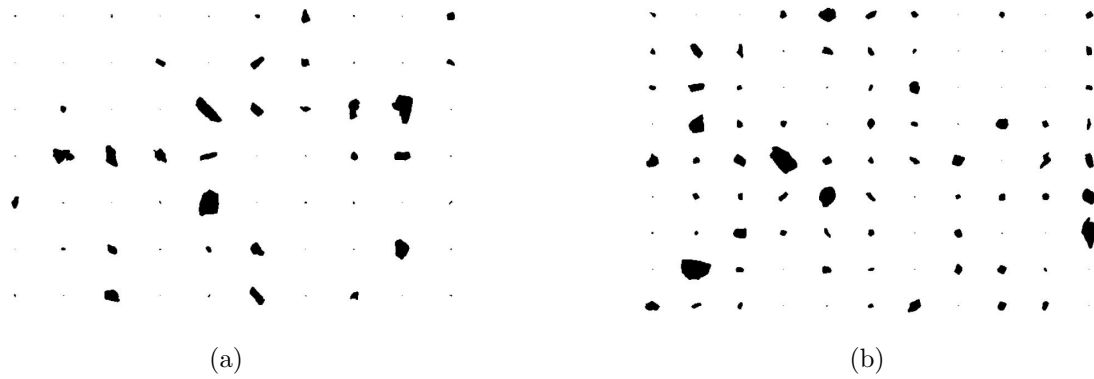


Figure 4.7.: QicPic image analysis of PEG ground for 3 minutes (a) and 5 minutes (b).

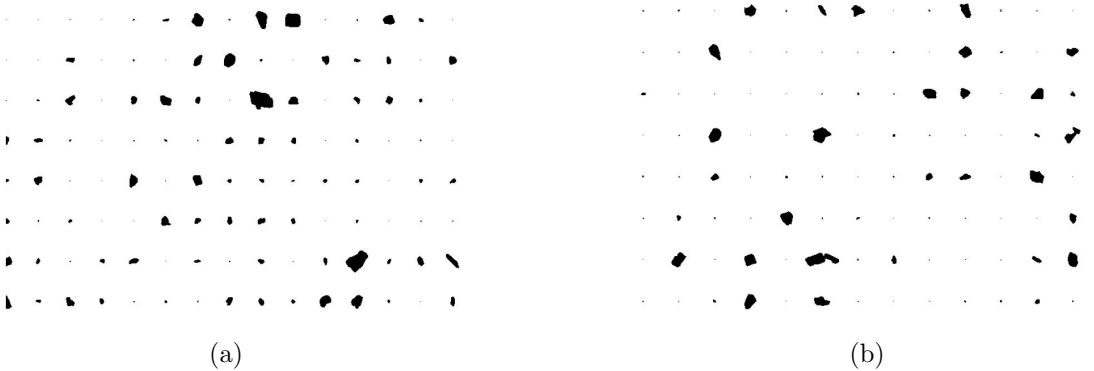


Figure 4.8.: QicPic image analysis of PEG ground for 7 minutes (a) and 10 minutes (b).

### 4.1.3. Surface Area

The measurement of the specific surface area, the pore volume and pore diameter of the bulk material was carried out for Lot native, Lot 3 and Lot 10 with 3 different samples each. The results in terms of average value and standard deviation are summed up in Table 4.5.

| Sample     | BET surface<br>[m <sup>2</sup> /g] | Total pore volume<br>[cm <sup>3</sup> /g] | Pore diameter<br>[nm] |
|------------|------------------------------------|---|-----------------------|
| Lot native | 0.049 ± 0.005                      | 0.0002 ± 0.00005                          | 16.5 ± 0.1            |
| Lot 3      | 0.215 ± 0.034                      | 0.00130 ± 0.00050                         | 23.2 ± 6.1            |
| Lot 10     | 0.340 ± 0.025                      | 0.00150 ± 0.00009                         | 17.7 ± 1.0            |

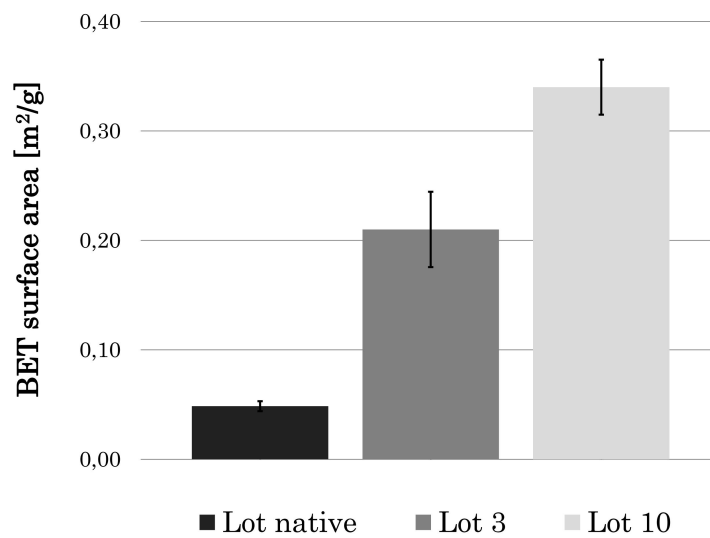
Table 4.5.: Particle properties from *ASAP* measurements.

Figure 4.9.: Specific surface area of 3 different lots of PEG.

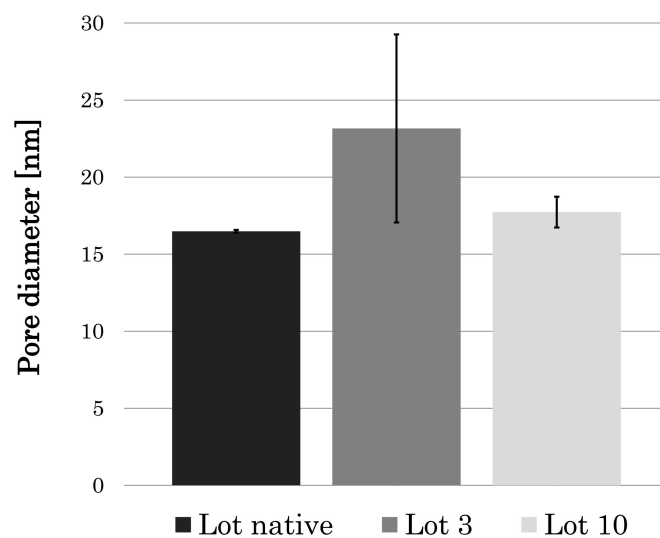


Figure 4.10.: Pore diameter of 3 different lots of PEG.

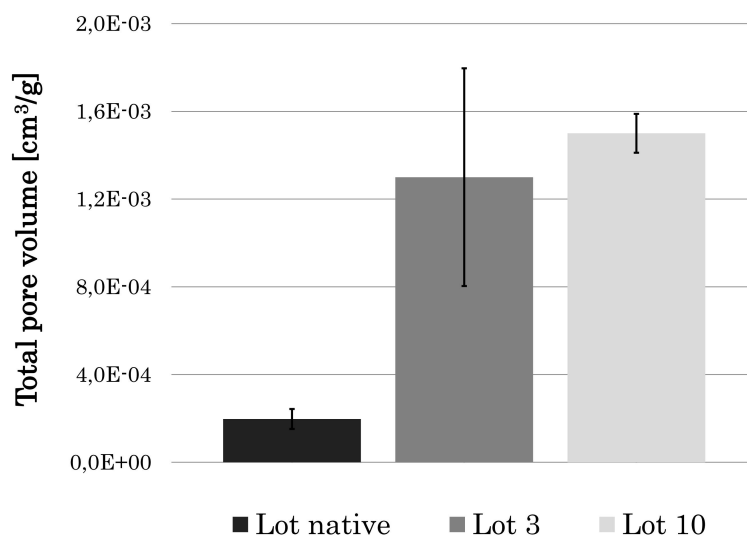


Figure 4.11.: Total pore volume of 3 different lots of PEG.

### Specific Surface Area

As expected, decreasing the particle size resulted in increased specific surface area of the particles, which confirmed the inverse relationship between particle size and surface area [42]. Native PEG showed a specific surface area of  $0.046 \text{ cm}^2/\text{g}$ , whereas the value increased to  $0.215 \text{ cm}^2/\text{g}$  for Lot 3 and to  $0.340 \text{ cm}^2/\text{g}$  for Lot 10.

### Pore Diameter

With regards to the pore diameter, all samples showed values between  $2 \text{ nm}$  and  $50 \text{ nm}$ , therefore classified as mesopores according to Webb and Orr [42]. The pore diameters of Lot native and Lot 10 were in the same order of magnitude, namely  $16.6 \text{ nm}$  and  $17.5 \text{ nm}$ , while Lot 3 differed by presenting a higher value of  $23.2 \text{ nm}$ . However, the standard deviation of Lot 3 was significantly greater and indicated measuring inaccuracy. In general, a change of particle size did not necessarily alter the pore diameter.

The measurement of the samples with different particle size resulted in significantly lower total pore volume for native PEG, namely  $0.0002 \text{ cm}^3/\text{g}$ , having almost the same values for Lot 3 and Lot 10, namely  $0.00130 \text{ cm}^3/\text{g}$  and  $0.00150 \text{ cm}^3/\text{g}$ . This fact correlates to the statement that milling and grinding procedures generate cracks, cavities and holes, all together called pores [42], which result in increased total pore volume.

## 4.1.4. Powder Rheology

### Stability Test

The stability test was performed for Lot native and Lot 10 (see Figure 4.12). Lot 10 presented higher stability, indicated by less variations in total energy and, consequently, a higher stability index compared to Lot native:

*Lot native:*     $\text{SI} = 0.846$

*Lot 10:*         $\text{SI} = 0.890$

Due to insufficient stability of Lot native, the wall friction and shear cell tests were performed for Lot 3 and Lot 10 only.

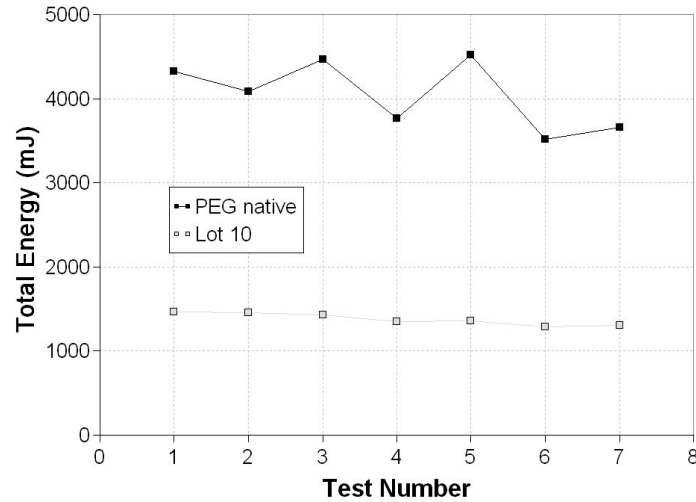


Figure 4.12.: Stability test for Lot native and Lot 10.

### Compressibility Test

The compressibility test was performed for Lot native, Lot 3 and Lot 10. For the last two lots, the test sequence was repeated once, using fresh and untreated material. All lots showed moderate compressibility (see Figure A.1) implying some cohesive properties, typical for most types of powders, were also observable here [10].

Lot 10 had the highest CI, representing the sample with the highest compressibility, followed by Lot 3 and Lot native, which had the same value for CI (see Table 4.6). The same trend could be seen for the conditioned bulk density, having the highest value for Lot 10 and decreasing with increasing particle size of the bulk material (see Table 4.6). The presented values are averaged results from the repeated measurements.

| Lot        | Compressibility index [-] | Conditioned bulk density [g/ml] |
|------------|---------------------------|---------------------------------|
| Lot native | 1.060                     | 0.592                           |
| Lot 3      | 1.060                     | 0.626                           |
| Lot 10     | 1.085                     | 0.634                           |

Table 4.6.: Compressibility indices and conditioned bulk densities of different lots of PEG.

### Wall Friction

The wall friction angle was determined using a 316 stainless steel disk with a surface roughness of  $0.28 \mu\text{m}$ . The test sequence was performed for Lot 3 and Lot 10, each repeated once, using fresh and untreated material. As shown in Table 4.7, Lot 10 showed a higher value for the wall friction angle in comparison to Lot 3. The values are averaged results from the repeated measurements.

| Lot    | Wall friction angle [°] |
|--------|-------------------------|
| Lot 3  | 13.8                    |
| Lot 10 | 16.4                    |

Table 4.7.: Wall friction angles of different lots of PEG.

The corresponding diagram, representing the stresses during analysis and used for the determination of the wall friction angle, can be found in Appendix A.2.2.

## 4.2. Dissolution Experiment

### 4.2.1. Dissolution in a Lab-Scale Tank

In order to investigate the dissolution behavior and kinetics of PEG in water, bulk material was fed and dissolved into a lab-scale stirred tank filled with deionized water. The time evolution of concentration was measured using a MIR-probe.

#### Calibration of the MIR-System

For analyzing the spectral information obtained from the dissolution experiments, a calibration of the MIR-system was carried out. The spectral data were evaluated as described in section 3.3. According to this, a regression line was plotted (see Figure 4.13), and used for further calculations of the concentration of the PEG solutions.

The following Equation (4.2) was used for calculating the concentration of the PEG solutions from the spectral data:

$$y = 0.0013 \cdot x - 0.0012 \qquad R^2 = 0.98972 \qquad (4.2)$$

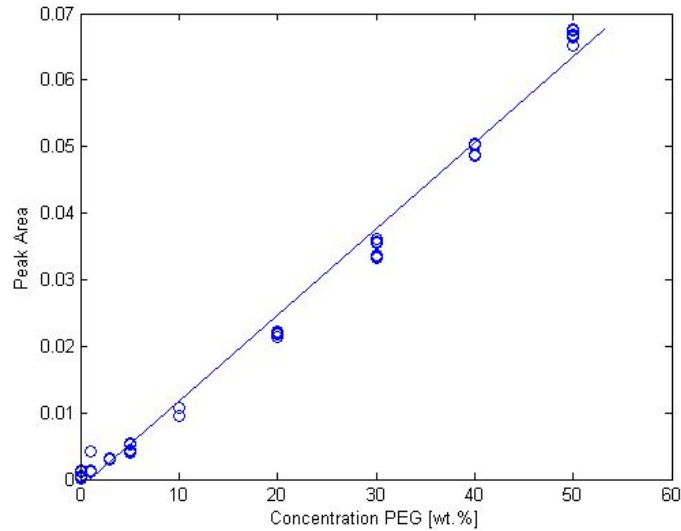


Figure 4.13.: Calibration fit used for evaluation of spectral data.

### Cleaning of the Probe

In order to verify the existence of potential contaminations, due to bulk material or solution, having an influence on signal and spectral data, the probe was cleaned at the end of dissolution step 5. Operatively, the probe was rinsed with deionized water, wiped with a tissue and dried. Afterwards, 10 spectra of the same solution were re-collected. This was performed at the end of the dissolution experiments of Lot 10 and Lot 3.

As shown in Figure A.3, just a little variation was observable in the measured values of the concentration before and after the cleaning procedure. The concentration of Lot 3 deviates by 0.8 % and that from Lot 10 by 0.4 % from the values before cleaning.

### Influence of Particle Size on Dissolution Behavior

The dissolution experiment was performed for two different lots of PEG, namely Lot 3 and Lot 10. For reasons of reproducibility, the experiment was repeated for each lot. The dissolution profiles, from the point where feeding was completed until the point where a constant concentration was reached, were normalized and plotted in the same diagram (see Figure 4.14). Here, the solid line represents the dissolution profiles of Lot 3, the dotted line those of Lot 10,  $c_t$  is the actual concentration of the solution at time step  $t$ , and  $c_{end}$  is the concentration where no changes were observable anymore, thus

the solution was regarded to be homogeneous.

One can recognize a slowdown of dissolution rate with increasing concentration of the solutions from step 1 to step 5. In addition, slower dissolution behavior is observable for Lot 3, representing the bulk material with larger particle sizes. This trend is not apparent at the two first dissolution steps, but becomes remarkable at steps 3, 4 and 5 (see also Figures 5.4, 5.5 and 5.6). Considering step 4, it is remarkable that Lot 10 shows a decreased dissolution rate during the first two minutes of dissolving. One assumes that this behavior arises from poor wetting of the particles. Since the powder was fed very fast, the formation of powder layers on the liquid surface was observable, particularly at high concentrations, therefore high viscosity of the solutions. Besides, slow wetting resulted in the formation of lumps, that increased dissolution time as well. One would expect this behavior at even higher concentrations, but it was not noticeable at step 5. Hence, the manner of feeding was not exactly the same and may significantly influence the dissolution behavior.

The evaluation of the dissolution profiles was only performed for the repeated measurements, since the data obtained from the first experiment were not analyzable due to air bubbles and particles interrupting the signal.

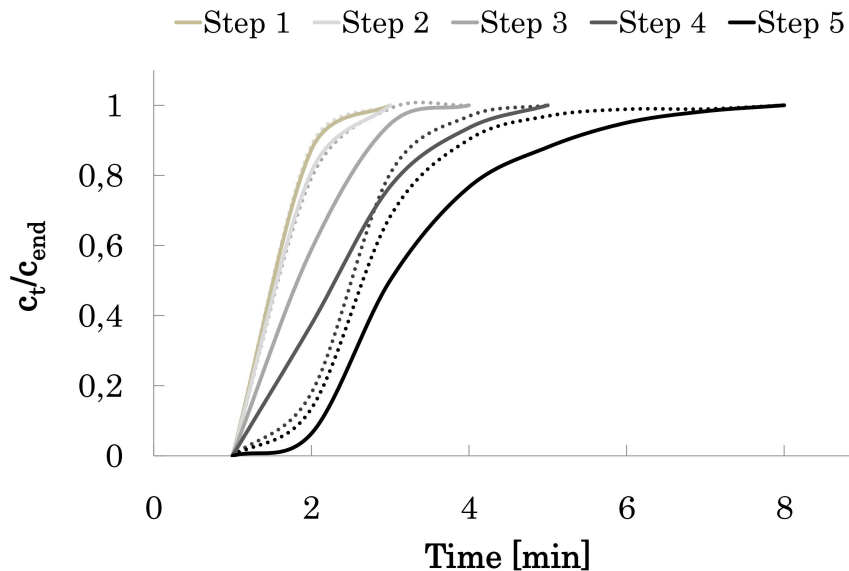


Figure 4.14.: Normalized dissolution profiles of steps 1-5; the solid line representing Lot 3, the dotted line Lot 10; impeller speed of 150 rpm.

### Influence of Impeller Speed on Dissolution Behavior

The same experiments were performed with a decreased impeller speed of 90 rpm. The total mass of PEG was fed in 4 instead of 5 steps, 60 g per step.

Regarding the dissolution profiles of these experiments, significant peaks were observed at the beginning of almost every dissolution step, see Figure 4.15. It is assumed that those peaks arose from air bubbles located at the head of the probe. Otherwise, this could have been the result of solid particles laid down on the probe and therefore adulterating the measured signal. Hence, the results can not be evaluated seriously and are not usable to be compared with those from the experiment with higher impeller speed. Apparently, a stirring rate of 90 rpm caused a flow field where particles and air bubbles were in such slow motion that they could adhere to the probe. Changing the position of the probe within the tank may alter the flow field and possibly prevents this phenomenon.

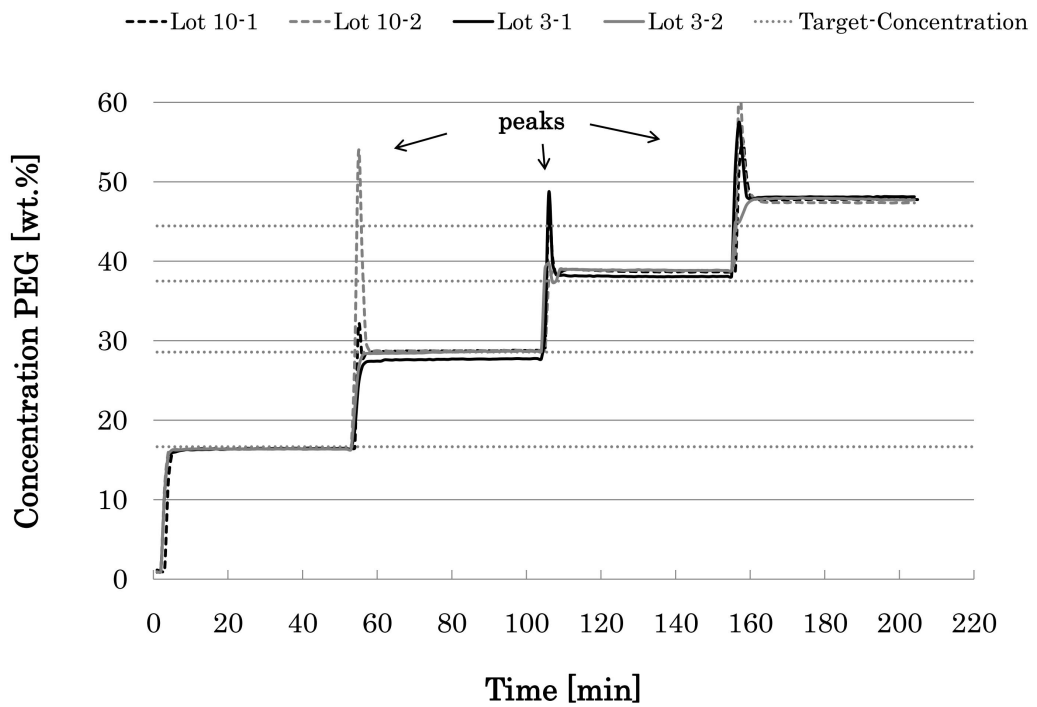


Figure 4.15.: Dissolution profiles of Lot 3 and Lot 10 at 90 rpm.

### **Precision and Reliability of the Measurements**

For evaluating the precision and the reliability of the MIR measurements, the dissolution profiles of Lot 3 and Lot 10, both measured two times at a stirring rate of 150 rpm, were compared. For this purpose, the last 15 data points from each dissolution step, where no change of concentration was observable anymore and the target concentration had been reached, were averaged (see Figure A.4). The **precision** of the measurement, meaning the dispersion about the averaged value of the 4 dissolution profiles, varied depending on the dissolution step, as shown in Table A.2. The averaged relative standard deviation of all steps amounts to 2.2 %.

The **reliability** of the measurements, meaning the dispersion of the average values from the real value, thus the target concentration of the PEG-solutions, also changed depending on the dissolution step. The average deviation from the measured concentration to the expected concentration was equal to 3.9 % (see Table A.3 and Figure A.5).

## **4.3. Analysis of Solution Properties**

### **4.3.1. Density**

The densities of the standard solutions of PEG in water were measured twice and the mean values were calculated, as presented in Table A.4 (Appendix). Plotting the density as a function of the concentration results in a linear increase with increasing concentration of the PEG solutions (see Figure 4.16).

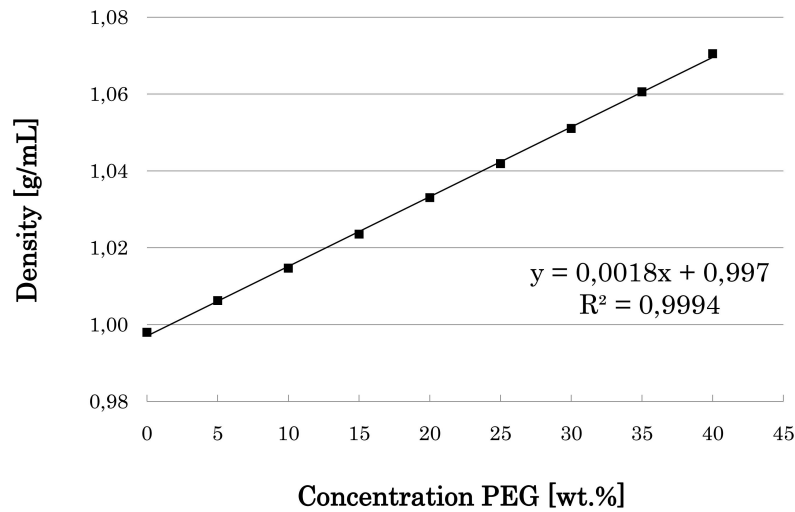


Figure 4.16.: Density of the PEG solutions.

### 4.3.2. Viscosity

The dynamic viscosity of the standard solutions was determined twice and the resulting values were averaged (see Table A.5). An exponential increase with increasing concentration of the PEG solutions was observable (see Figure 4.17).

Afterwards, the kinematic viscosity was calculated through the following relationship (see Table A.5):

$$\nu = \frac{\mu}{\rho} \quad (4.3)$$

where  $\nu$  is the kinematic viscosity [ $mm^2/s$ ],  $\mu$  is the dynamic viscosity [ $mPa \cdot s$ ] and  $\rho$  is the density [g/ml] of the PEG solutions.

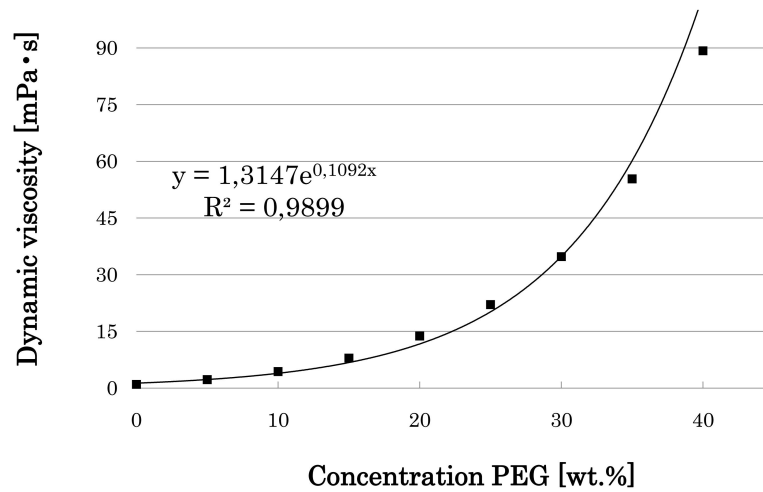


Figure 4.17.: Dynamic viscosity of the PEG solutions.

### 4.3.3. Saturation Concentration

The identification of the saturation point was performed visually and found to be within a concentration range between 55.5 wt.% and 56.1 wt.%. Here, the solutions turned out to be clear and no particles were visible anymore (see Table<sup>1</sup> 4.8).

| Mass PEG [g] | Concentration PEG [wt.%] | Comment                       |
|--------------|--------------------------|-------------------------------|
| 39.1         | 61.0                     | turbid, particles observable  |
| 34.5         | 58.0                     | turbid, no particles visible  |
| 31.9         | 56.1                     | turbid, no particles visible* |
| 31.2         | 55.5                     | clear, no particles visible*  |
| 30.6         | 55.0                     | clear, no particles visible*  |

Table 4.8.: Analysis of the saturation concentration of PEG in water.

<sup>1</sup>The analysis of the saturation concentration of the samples labeled \* was performed twice.

# 5. Dissolution Model

According to the experiments performed in the laboratory, the development of a mathematical model was established in order to characterize and understand the dissolution process. Furthermore, the model was used to compare and verify the experimental data obtained from the dissolution experiment. The conditions chosen to calculate the mass transfer occurring during the dissolution of PEG in water were the same as presented in chapter 4.

Some variables and parameters, like particle size and viscosity of the solutions, were directly taken from the experimental results, while others, e.g. the diffusion coefficient, were values found in literature.

## 5.1. Mass Transfer Equations

The mass transfer of the particles from the solid to the liquid phase can be calculated from the following equation [21]

$$\dot{M} = A \cdot \beta \cdot \Delta\rho = A \cdot \beta \cdot (\rho^* - \rho^\infty) \quad (5.1)$$

where  $A$  is the total surface area of the particles [ $m^2$ ],  $\beta$  is the mass transfer coefficient [ $m/s$ ],  $\rho^*$  is the density of the saturated solution [ $kg/m^3$ ] and  $\rho^\infty$  is the local density of the solution [ $kg/m^3$ ].

The total surface area of the particles  $A$  can be calculated via the particle diameter  $d_p$  and the number of particles  $z_p$ , which can be derived from the total particle mass and is given by

$$A = z_p \cdot A_p = z_p \cdot \pi \cdot d_p^2 \quad (5.2)$$

The mass transfer coefficient  $\beta$  depends on the Sherwood number  $Sh$ , the particle

diameter  $d_p$ , and the bulk diffusion coefficient  $D$  of PEG in water:

$$\beta = \frac{Sh \cdot D}{d_p} \quad (5.3)$$

According to KRISCHER and KAST the Sherwood number for laminar and turbulent flow for  $10 \leq Re \leq 10^7$  and  $0.7 \leq Sc \leq 70000$  can be calculated by the following equation

$$Sh = Sh_{min} + \sqrt{Sh_{lam}^2 + Sh_{turb}^2} \quad (5.4)$$

where  $Sh_{min}$  depends on the geometry of the body, having the following magnitudes for a

|          |                  |
|----------|------------------|
| Sphere   | $Sh_{min} = 2$   |
| Cylinder | $Sh_{min} = 0.3$ |
| Plate    | $Sh_{min} = 0$   |

The Sherwood number for laminar conditions according to POHLHAUSEN is defined by

$$Sh_{lam} = 0.664 \cdot \sqrt{Re_{L'}} \cdot Sc^{1/3} \quad (5.5)$$

while for turbulent conditions the relation from PETUKHOV and POPOV can be used

$$Sh_{turb} = \frac{0.037 \cdot Re_{L'}^{0.8} \cdot Sc}{1 + 2.443 \cdot Re^{-0.1} \cdot (Sc^{2/3}) - 1} \quad (5.6)$$

Here,  $Re$  is the dimensionless Reynolds number, given by

$$Re = \frac{v_{rel} \cdot L'}{\nu} \quad (5.7)$$

where  $v_{rel}$  is the relative velocity between the fluid and the particles [ $m/s$ ],  $\nu$  the kinematic viscosity of the fluid [ $m^2/s$ ] and  $Sc$  the Schmidt number defined by

$$Sc = \frac{\nu}{D} \quad (5.8)$$

with  $D$  as bulk diffusion coefficient of PEG in water.

In order to calculate the Sherwood numbers for laminar and turbulent conditions, as well as the Reynolds number, a characteristic length  $L'$ , related to the geometry of the body that is overflowed, is needed. According to KRISCHER and KAST,  $L'$  is given by

$$L' = \frac{A}{U} = \frac{d_p^2 \cdot \pi}{d_p \cdot \pi} = d_p \quad (5.9)$$

where  $U$  is the circumference of the particle orthogonal to the flow direction of the fluid.

In this study, the PEG particles were assumed to be spheres, leading to a characteristic length equal to the diameter of the particles ( $L' = d_p$ ).

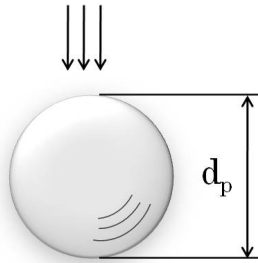


Figure 5.1.: Characteristic length of a sphere to be overflowed by a fluid.

The relative velocity between the fluid and the particles  $v_{rel}$ , can be defined according to Kolmogorov as

$$v_{rel} \approx \pi \cdot n \cdot d \cdot \left(\frac{d_p}{d}\right)^{1/3} \quad (5.10)$$

where  $n$  is the rotation speed of the impeller and  $d$  is the diameter of the impeller blades.

The diffusion coefficient for polyethylene glycol in water at 25°C can be calculated according to Singh et al. [5] using the following equation

$$D = 1.465 \cdot 10^{-4} \cdot M_a^{-0.557} \quad [cm^2/s] \quad (5.11)$$

where  $M_a$  is the average molecular weight of PEG, having the value of 6000  $g/mol$ .

## 5.2. Calculation of the Dissolution Model

For calculating the averaged mass transfer of PEG in water, the mass flow was approximated in several steps and related to the starting values. The subscript  $0$  refers to starting conditions, where no PEG is dissolved, while the subscript  $t$  indicates the corresponding value at a given time step. The time-dependent magnitudes can then be calculated as follows.

The time-dependent total surface area of the particles  $A_t$  is given by

$$\frac{A_t}{A_0} = \left( \frac{d_{pt}}{d_{p0}} \right)^2 \quad (5.12)$$

The decrease of the particle diameter is illustrated in Figure 5.2.

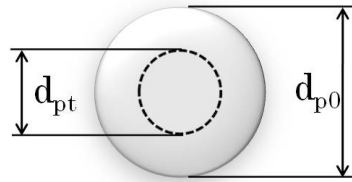


Figure 5.2.: Decrease of particle diameter as a function of time.

The Reynolds number at a given time step  $Re_t$  is given by

$$\frac{Re_t}{Re_0} = \left( \frac{\nu_0}{\nu_t} \right) \cdot \left( \frac{d_{pt}}{d_{p0}} \right)^{4/3} \quad (5.13)$$

The relative velocity according to KOLMOGOROV at time  $t$  follows

$$\frac{v_{rt}}{v_{r0}} = \left( \frac{d_{pt}}{d_{p0}} \right)^{1/3} \quad (5.14)$$

The Sherwood number, reduced to laminar flow conditions as  $Re < 10^5$ , is given by

$$Sh_{lam} = 0.664 \cdot \sqrt{Re_{L'}} \cdot Sc^{1/3} \quad (5.15)$$

and the time-dependent Sh can be calculated according to

$$\frac{Sh_t}{Sh_0} = \left(\frac{\nu_t}{\nu_0}\right)^{1/3} \cdot \left(\frac{d_{p_t}}{d_{p_0}}\right)^{2/3} \cdot \sqrt{\frac{\nu_0}{\nu_t}} \quad (5.16)$$

The mass transfer coefficient  $\beta_t$  is then given by

$$\frac{\beta_t}{\beta_0} = \left(\frac{\nu_t}{\nu_0}\right)^{-1/6} \cdot \left(\frac{d_{p_t}}{d_{p_0}}\right)^{-1/3} \quad (5.17)$$

and the mass flow at a given time step t can be calculated according to

$$\dot{M}_t = A_0 \cdot \beta_0 \cdot \left(\frac{d_{p_t}}{d_{p_0}}\right)^{5/3} \cdot \left(\frac{\nu_t}{\nu_0}\right)^{-1/6} \cdot (\rho^* - \rho_t^\infty) \quad (5.18)$$

Afterwards, the decrease of the particle diameter as a function of time can be derived from the primary particle mass,  $m_{p_0}$ , and the mass of particles being dissolved at time step t,  $m_{p_t}$ :

$$\frac{d_{p_t}}{d_{p_0}} = \left(\frac{m_{p_0} - m_{p_t}}{m_{p_0}}\right)^{1/3} \quad (5.19)$$

Hence,  $(m_{p_0} - m_{p_t})$  is the mass of undissolved particles remaining in the solution. The decrease of mass was approximated in 100 steps and, finally, the dissolution time per step was calculated according to

$$\Delta t = \frac{m_{p_t}}{\overline{\dot{M}}_t} \quad (5.20)$$

where  $\overline{\dot{M}}_t$  is the averaged mass transfer from time step  $i$  to time step  $i + 1 < 100$  and given by

$$\overline{\dot{M}}_t = \frac{1}{2} \cdot (\overline{\dot{M}}_{t(i)} + \overline{\dot{M}}_{t(i+1)}) \quad (5.21)$$

### Parameters for the Calculation of the Dissolution Model

The dissolution profiles were calculated according to the experiments in the lab. It was assumed that PEG was fed into a stirred tank filled with 300 ml of water in 5 steps. The amount of PEG for each step was equal to 60 g and as soon as the bulk material had been dissolved, another 60 g were fed to the same solution in a next step. The dissolution profiles were calculated until 99 % of the total mass of each step were dissolved. The saturation concentration was assumed to be 55.5 wt.%, according to the experimental results presented in section 4.3.3. The particle diameters used for the calculation were 63.8  $\mu\text{m}$  for Lot 3 and 50.6  $\mu\text{m}$  for Lot 10. The diffusion coefficient for PEG in water at 25°C was calculated according to Equation 5.11 and amounted to  $1.15 \cdot 10^{-10} \text{ m}^2/\text{s}$ . The impeller speed was 150 rpm and the diameter of the blades 100 mm.

### Calculated Model

The calculated dissolution profiles are displayed in Figure 5.3. Here, the solid line represents the dissolution profiles of Lot 3 and the dotted line those of Lot 10. Table 5.1 shows the calculated dissolutions times of Lot 3 and Lot 10 for dissolving the same amount of PEG. The increasing concentration, thus viscosity, of the solutions is also presented in Table 5.1.

As expected, smaller particles and therefore major surface area results in higher mass transfer and faster dissolution, according to Equation 5.1. The increase of dissolution time with increasing concentration, or rather density, of the solution is also obvious as the difference  $(\rho^* - \rho^\infty)$  becomes smaller and therefore mass transfer is decelerated.

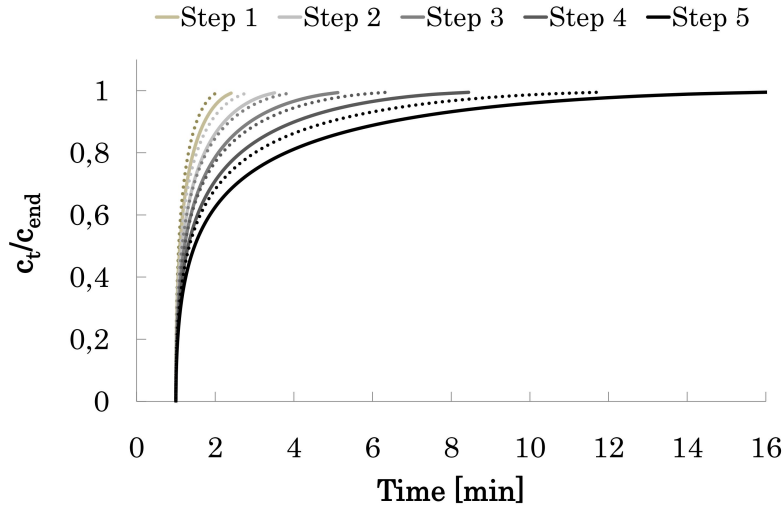


Figure 5.3.: Calculated dissolution profiles for Lot 3 and Lot 10.

| Step | Time [min] | Time [min] | $c_{end}$ [wt.%] |
|------|------------|------------|------------------|
|      | Lot 3      | Lot 10     |                  |
| 1    | 1.4        | 1.0        | 16.6             |
| 2    | 2.5        | 1.8        | 28.5             |
| 3    | 4.1        | 3.0        | 37.5             |
| 4    | 7.4        | 5.3        | 44.5             |
| 5    | 15.0       | 10.8       | 50.0             |

Table 5.1.: Dissolution times of Lot 3 and Lot 10.

### Comparison Model and Experiments

Comparing the calculated model to the experimental results, one can recognize a remarkable difference in dissolution time: the calculated dissolution profiles are characterized by a sharp increase in concentration at the beginning and slowly approximate the desired end-concentration. Considering the data from the experiments, one can see slower initial dissolution behavior, nevertheless the end-concentration is reached rapidly.

There are several explanations for this kind of behavior:

- The MIR-system limited the measurement of the concentration to one data point per minute, which is especially at the beginning of the dissolution process not sufficient to accurately follow the change in concentration.
- The model assumes perfect wetting of every single particle, which could not be realized under the experimental conditions. Hence, poor wetting, high feeding rate and subsequent lump formation decelerate dissolution.
- In the model the PEG particles were assumed to be perfect spheres which was not confirmed in the experiments.

Nevertheless, the simple mathematical model appeared to reproduce in a satisfactory way the dissolution time for different feeding steps. Therefore, this approach could be used as engineering tool to up-scale and design dissolution equipments.

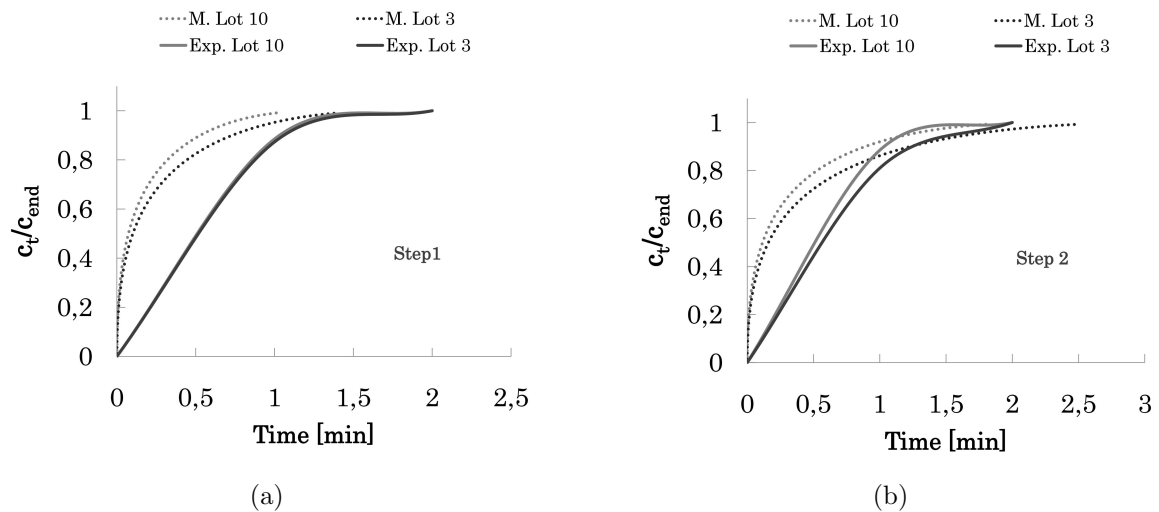


Figure 5.4.: Experimental (Exp.) and modelled (M.) dissolution profiles of Step 1 (left) and Step 2 (right).

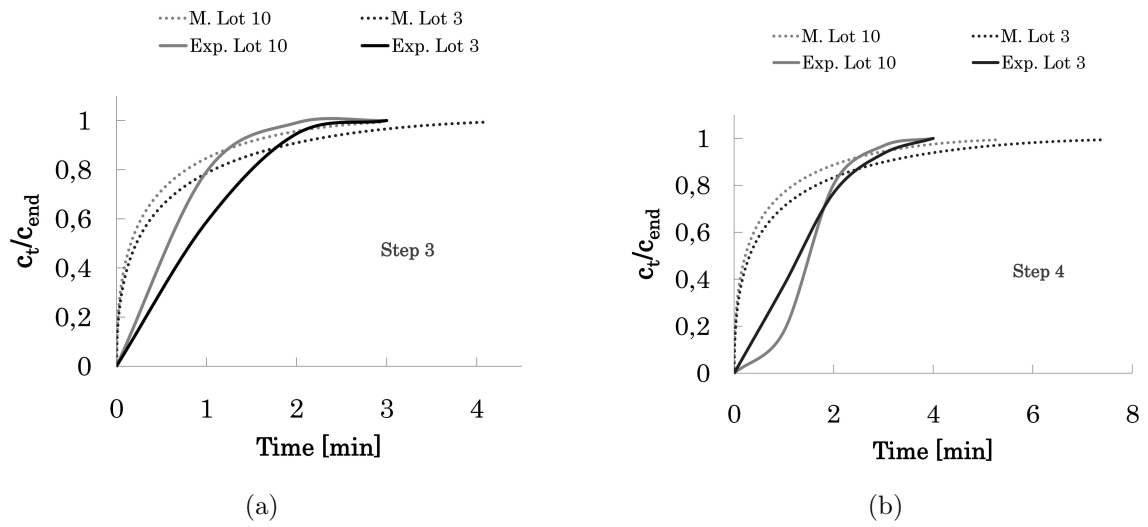


Figure 5.5.: Experimental (Exp.) and modelled (M.) dissolution profiles of Step 3 (left) and Step 4 (right).

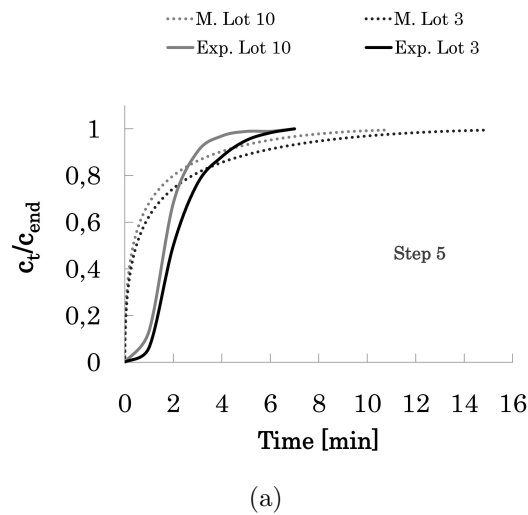


Figure 5.6.: Experimental (Exp.) and modelled (M.) dissolution profiles of Step 5.

## 6. Hopper Design

Two important design criteria have to be considered when constructing a hopper: the minimum hopper angle  $\Theta$ , in order to assure mass flow, and the hopper outlet size  $B$ , to avoid any blockage due to arching (see Figure 6.1). The hopper is defined to be the lower converging section of a silo and the hopper angle, also called conus angle, is the angle between the converging and the horizontal section [8].

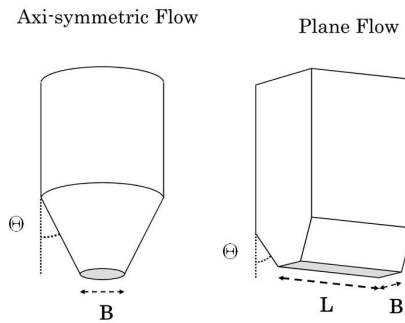


Figure 6.1.: Conus angle and hopper outlet size of a conical and a plane flow hopper [10].

The data required for calculating the hopper angle and the outlet size were derived from the rheological tests described in section 3.2.5, and performed for Lot 3 and Lot 10.

### 6.1. Conus Angle

For calculating the conus angle of a hopper, the wall friction angle  $\varphi_w$  of the material used and the effective angle of internal friction  $\varphi_e$  have to be known. The material used during the wall friction tests was a 316 stainless steel disk with a surface roughness of  $0.28 \mu m$ .

The conus angle required to assure mass flow conditions, may be then determined using  $\varphi_w$ -  $\Theta$  - diagrams or it can be calculated according to ter Borg [2] by

$$\Theta_c \leq 90^\circ - \frac{1}{2} \cdot \arccos \cdot \frac{1 - \sin\varphi_e}{2 \cdot \varphi_e} - \frac{\varphi_w}{2} - \frac{1}{2} \cdot \arcsin \cdot \frac{\sin\varphi_w}{\sin\varphi_e} \quad (6.1)$$

for conical hoppers and by

$$\Theta_p \leq \left(60.5^\circ + 6.636 \cdot 10^{-2} \cdot \arctan \cdot \frac{50^\circ - \varphi_e}{7.73}\right) \cdot \left(1 - \frac{\varphi_w}{42.3 + 0.131 \cdot e^{(0.06 \cdot \varphi_e)}}\right) \quad (6.2)$$

for plane flow geometries.

The resulting values for the conus angles for Lot 3 and Lot 10, calculated using the equations above, can be found in Table 6.1. They represent the maximum conus angles not to be exceeded in order to avoid core flow. A safety margin of  $3^\circ$  was subtracted from the calculated values in order to ensure mass flow under all operating conditions.

| Lot    | $\Theta_c$ [°] | $\Theta_p$ [°] |
|--------|----------------|----------------|
| Lot 3  | 30.8           | 39.5           |
| Lot 10 | 27.8           | 36.2           |

Table 6.1.: Calculated conus angles for conical and plane flow hoppers.

## 6.2. Hopper Outlet Size

Considering the design of the hopper outlet size, one has to keep in mind the stresses developing within the silo. Powders exposed to compaction develop stresses that increase with an increase in compaction stress. This is only true for cohesive powders, as free-flowing powders do not develop strength under increasing compaction stresses, thus flow will always occur.

### Critical Flow Conditions

In order to assure powder flow driven by gravity, the stresses developed by cohesive powders under the influence of compaction may not be greater than the stresses acting

within the surface of an arch. In this case, the stresses developed by the powder are not sufficient to cause obstruction. The relationship between compacting stresses in a hopper and stresses developed within the powder bulk is defined by the hopper flow factor  $ff$  and given by [29]

$$ff = \frac{\sigma_c}{\sigma_D} = \frac{\text{compacting stress in the hopper}}{\text{stress developed within the powder}} \quad (6.3)$$

The hopper flow factor depends on the nature of the solid, the wall material and the slope of the hopper wall, and can be determined graphically from *flow factor charts* according to Jenike [18]. Great values of  $ff$  indicate low flowability, including high compacting stresses. [29]

Hence, the limiting condition for powder flow is given by a straight line of slope  $1/ff$  in a  $\sigma_c/\sigma_y$ -plot (see Figure 6.2). Adding the powder flow function to the same diagram, a flow/no flow criterion,  $\sigma_{crit}$  can be set up [29]:

$$\begin{aligned} \text{actual stress developed} < \sigma_{crit} &\rightarrow \text{no flow} \\ \text{actual stress developed} > \sigma_{crit} &\rightarrow \text{flow} \end{aligned}$$

The powder flow function, which is only a function of the powder properties, is obtained by plotting pairs of  $(\sigma_c - \sigma_y)$  values from each yield locus, derived from the shear cell measurements, against each other. Therein,  $\sigma_y$  is the unconfined yield stress of the powder, which is the stress that causes the powder flow. If the stress developed in the surface of the arch  $\sigma_D$  is greater than the unconfined yield stress  $\sigma_y$ , flow will occur:  $\sigma_D > \sigma_y$ .

The critical stress value  $\sigma_{crit}$  indicating flow or no flow can be derived from the intersection of the hopper flow function and the powder flow function and reveals the stress developed within the arch.

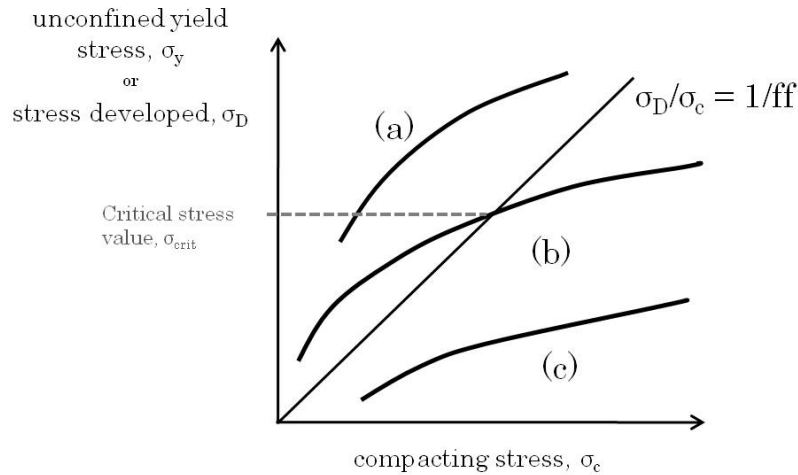


Figure 6.2.: Hopper and powder flow functions for determination of critical stress developed within the powder [29].

Figure 6.2 shows three different kinds of powder flow functions and flow behaviors, respectively. Function (a) develops a yield stress greater than  $\sigma_c/ff$  and therefore no flow will occur. In contrast, function (c) develops stresses less than  $\sigma_c/ff$ , hence flow will always occur without the formation of an arch. Considering flow function (b), there is a critical stress value,  $\sigma_{crit}$  indicating the critical stresses responsible for flow or no flow behavior of the powder.

### Calculation of Hopper Outlet Size

In order to avoid arching and to allow mass flow, the minimum outlet size of a conical hopper can be calculated according to Rhodes [29] by

$$B_c = \frac{H_c(\Theta) \cdot \sigma_{crit}}{\rho_{B,crit} \cdot g} \quad (6.4)$$

and for a plane flow hopper by

$$B_p = \frac{H_p(\Theta) \cdot \sigma_{crit}}{\rho_{B,crit} \cdot g} \quad (6.5)$$

$B_c$  and  $B_p$  are the critical diameter and width of the hopper outlet, respectively,  $H(\Theta)$  is a factor determined by the slope of the hopper wall with a conus angle  $\Theta$ ,  $\sigma_{crit}$  is

the critical stress developed in the surface of an arch,  $\rho_{B,crit}$  is the critical bulk density under flow conditions and  $g$  is the acceleration due to gravity.

For mass flow, the factor  $H(\Theta)$  should be equal to  $H_c(\Theta) = 2.2$  for a conical hopper and to  $H_p(\Theta) = 1.35$  for a plane flow hopper [37].

Evaluating the data obtained from the rheological tests of Lot 3 and Lot 10 by plotting the powder and hopper flow functions in the same diagram, one obtains yield stresses that are always lower than  $\sigma_c/ff$ . This indicates that no critical stress value  $\sigma_{crit}$  exists and that flow occurs without any limiting condition (see Figure 6.3).

The hopper flow functions were derived from the *flow factor charts* for an effective angle of internal friction of  $\varphi_e = 50^\circ$  and a wall friction angle of  $\varphi_w = 13.8^\circ$  for Lot 3 and  $\varphi_w = 16.4^\circ$  for Lot 10. The resulting flow factor functions were  $ff = 1.3$  for plane flow and  $ff = 1.4$  for flow in a conical hopper for both, Lots 3 and 10.

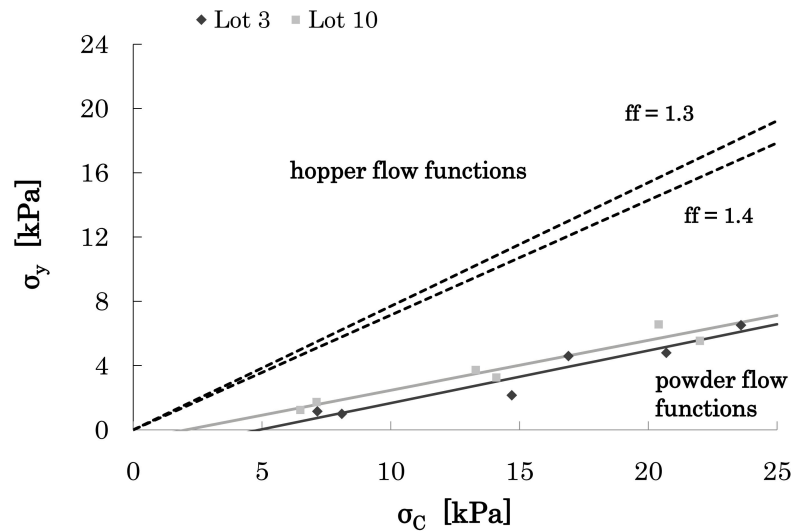


Figure 6.3.: Hopper flow functions and powder flow functions of Lot 3 and Lot 10.

### Influence of Particle Size

As there is no critical outlet size for the hopper depending on the stresses developed within the powder, the particle size determines the minimum outlet size in order to avoid arching. An arch may be formed by coarse particles due to interlocking, hence the outlet size is a function of the maximum particle size and given by

$$B_c = 10 \cdot x_{max} \quad (6.6)$$

for the diameter of a conical outlet  $B_c$  and by

$$B_p = 7 \cdot x_{max} \quad (6.7)$$

for the outlet width  $B_p$  of a plane flow hopper [37]. The maximum particle sizes, based on a  $Q_0$ -number distribution, were found to be 1100  $\mu m$  for Lot 3 and 700  $\mu m$  Lot 10. The corresponding hopper outlet sizes for conical and plane flow geometries were calculated and can be found in Table 6.2.

| Lot    | $B_c$ [cm] | $B_p$ [cm] |
|--------|------------|------------|
| Lot 3  | 1.1        | 0.8        |
| Lot 10 | 0.7        | 0.5        |

Table 6.2.: Calculated dimensions of outlet sizes for conical and plane flow hoppers.

As can be seen from the calculations of the conus angles and the critical outlet sizes, the discharge behavior of conical hoppers seems to be more unfavourable. In order to assure mass flow, the attention has to be turned on the surface properties of the wall material. A slight increase of the wall friction angle, for example caused by erosion or oxidation, can easily convert mass flow to core flow behavior. This is true if the hopper flow function, taken from the *flow factor charts*, is closely located to core flow behavior [37].

## 7. Conclusions

In this study, the physicochemical properties of granular PEG and the solution attributes of PEG dissolved in water were experimentally assessed. Therefore, the bulk material was broken up by milling and particle shape, size distribution and surface area were determined. Besides, powder rheology tests were performed in order to obtain the powder bulk properties and to calculate the critical dimensions for a hopper design. The solution attributes were investigated by means of density and viscosity as a function of concentration of PEG. The saturation concentration of PEG in water was analyzed as well.

In addition, the bulk material was fed into a lab-scale stirred tank to gain insight into the dissolution kinetics, as well as to investigate the influence of particle size and impeller speed on dissolution behavior.

Thereafter, a mathematical model was developed to describe and understand the mass transfer phenomena between solids and liquids. According to the results obtained from the rheological measurements, a hopper for storage and processing of granular PEG was designed.

From the milling experiments, two lots of PEG with distinct particle size were chosen: Lot 3, milled for 3 minutes in a ball mill, and Lot 10, indicated by an increased milling duration of 10 minutes and thus, smaller particle size.

The shape analysis of PEG displayed the particles as plane, elongated platelets, converting to more and more squarish forms with decreasing particle size distribution.

Considering the PSD, bulk material of Lot 3 offered a median particle size of  $x_{50} = 63.8 \mu m$ , whereas Lot 10 showed a decreased value of  $x_{50} = 50.6 \mu m$ . According to the specific surface area, this increased by decreasing PSD, and resulted in  $0.215 \text{ cm}^2/g$  for Lot 3, and  $0.340 \text{ cm}^2/g$  for Lot 10.

From the parameters obtained by the rheological tests, a conical hopper should be designed with a critical conus angle of  $\Theta_c = 30.8^\circ$  and a minimum outlet diameter of  $B_c = 1.1 \text{ cm}$  for Lot 3, being  $\Theta_c = 27.8^\circ$  and  $B_c = 0.7 \text{ cm}$  for Lot 10.

---

The analysis of the solution properties resulted in a linear increase of the density and an exponential rise of the dynamic viscosity with increasing concentration of PEG. In addition, the saturation concentration of PEG in water at 25°C was found to be 55.5 wt.%.

From the experimental data achieved by the dissolution experiments, it was possible to establish a relationship between particle size and dissolution rate. The decrease of dissolution rate at higher concentrations and therefore higher viscosity of the solutions was confirmed. As well, dissolution of smaller particles was faster, but this was only observable at high concentrations. The initial dissolution steps showed no dependency of dissolution rate on particle size. The influence of impeller speed on dissolution behavior was not analyzable, as the IR-signal was interrupted due to air bubbles and particles.

The dissolution model was able to confirm the correlation between dissolution time, particle size and concentration of the solution. However, the presented simple model did not completely match the experimental results, since it presumed ideal conditions and wetting behavior.

To conclude and sum up the results attained throughout this study for PEG particles and solutions, the following issues were observable:

- Particle size and polydispersity decreased with increasing milling duration;
- Specific surface area and pore volume of grains increased with decreasing particle size;
- Density increased linearly and dynamic viscosity exponentially with increasing concentration of PEG in water solutions;
- The saturation concentration of PEG in water was found to be 55.5 wt.%;
- A dependency of dissolution rates on particle size was detected at high concentrations: higher dissolution rate for smaller particles;
- Hopper Design: a correlation between critical dimensions and particle size was found, namely a higher conus angle and outlet size for greater particles;
- The dissolution model was able to replicate the dissolution behavior, but did not completely fit the experiments. Nevertheless, it can give a good approximation of dissolution times for engineering applications.

---

Further work should be done on the investigation of the dissolution kinetics, since not all results from the dissolution experiments were satisfying. With regard to measuring the time-dependent evolution of concentration, it is recommendable to use a system that could be capable of collecting data within shorter time intervals. Besides, the use of a conductivity probe or sampling for external analysis may be appropriate. The conductivity probe implies a conducting fluid, e.g. water, and solids that are non-conducting in order to measure the change in electrical conductivity as a function of increasing concentration. It is precise and accurate and well suited for laboratory-scaled investigations, but also has the drawback of being intrusive and hence alters the flow conditions within the vessel. Sampling is an alternative method, since standardized laboratory equipment (e.g. sieve analysis, UV-VIS spectroscopy) may be used for analysis. However, appropriate and representative sampling is a challenging task and may significantly influence the results. [26]

# A. Tables and Figures

## A.1. Particle Size Distribution

Settings of the QicPic Particle Size Analyzer used for measuring the particle size distributions.

| Frame rate [fps] | Primary Pressure [bar] | Vibration Power [%] | Funnel height [mm] | Trigger $C_{opt}$ [%]                             |
|------------------|------------------------|---------------------|--------------------|---|
| 450              | 0.1                    | 100                 | 1                  | Start: $C_{opt} > 0,01$<br>Stop: $C_{opt} < 0,01$ |

Table A.1.: Setting of parameters for QicPic analysis.

## A.2. Powder Rheology

### A.2.1. Compressibility Test

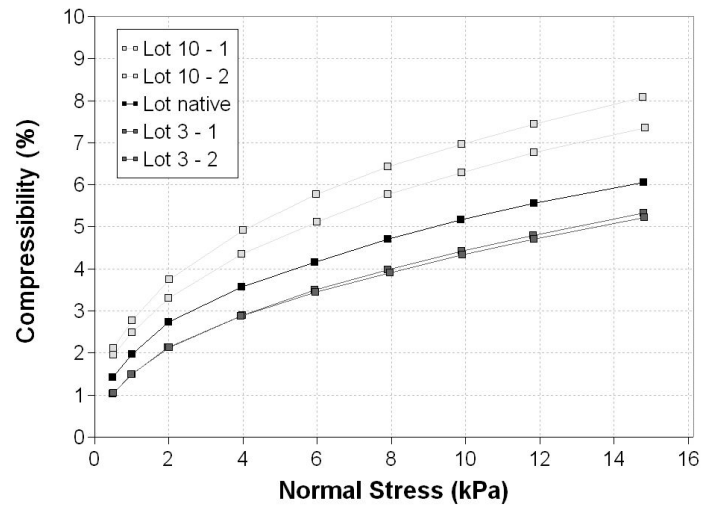


Figure A.1.: Compressibility of Lot native, Lot 3 and Lot 10.

### A.2.2. Wall Friction Test

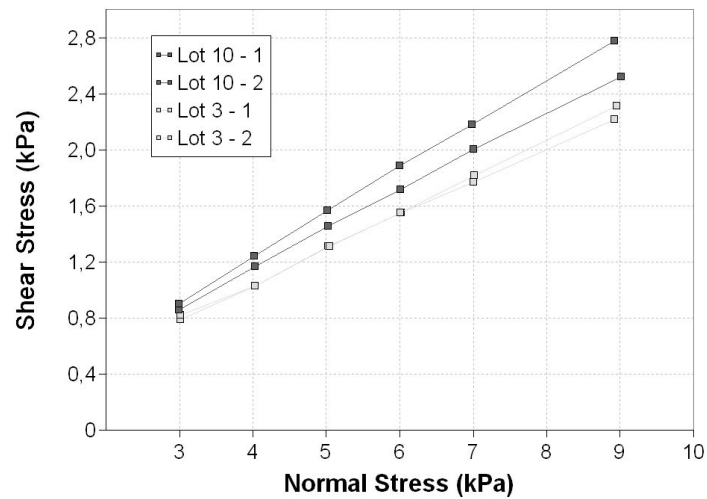


Figure A.2.: Steady-state shear stress against normal stress.

## A.3. Dissolution Experiment

### A.3.1. Cleaning of the Probe

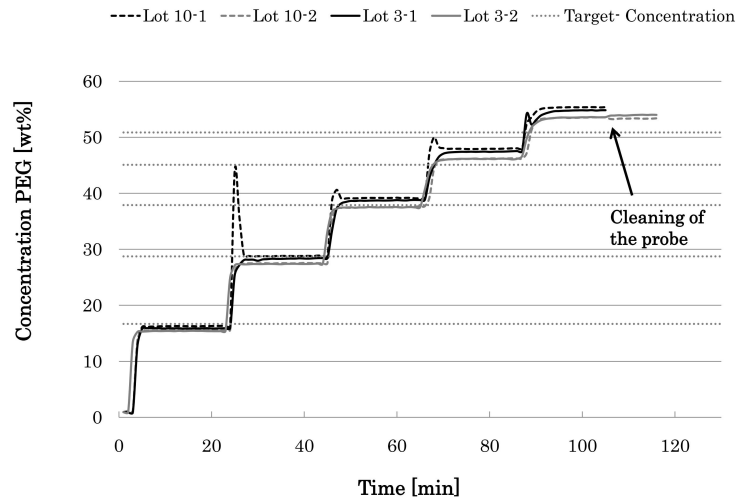


Figure A.3.: Dissolution profiles of Lot 3-2 and Lot 10-2 at 150 rpm.

### A.3.2. Precision and Reliability of MIR Measurements

| Dissolution step | $c_t$ [wt.%] | $c_a$ [wt.%] | Standard deviation [wt.%] | Relative standard deviation [%] |
|------------------|--------------|--------------|---------------------------|---------------------------------|
| 1                | 16.7         | 15.8         | 0.4                       | 2.4                             |
| 2                | 28.7         | 28.0         | 0.7                       | 2.4                             |
| 3                | 37.9         | 38.2         | 0.8                       | 2.2                             |
| 4                | 45.1         | 46.9         | 0.9                       | 2.0                             |
| 5                | 50.9         | 54.2         | 0.9                       | 1.7                             |

Table A.2.: Precision of the MIR measurements depending on the dissolution step,  $c_t$  - target concentration,  $c_a$  - averaged actual concentration.

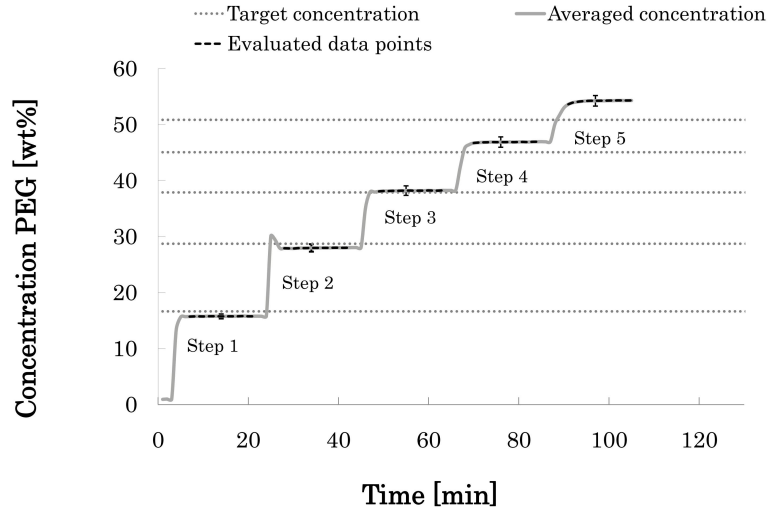


Figure A.4.: Precision and trueness of MIR measurements.

| Dissolution step | $c_t$ [wt.%] | $c_a$ [wt.%] | $(\frac{c_t - c_a}{c_t} \cdot 100)$ [%] |
|------------------|--------------|--------------|---|
| 1                | 16.7         | 15.8         | -5.3                                    |
| 2                | 28.7         | 28.0         | -2.7                                    |
| 3                | 37.9         | 38.2         | 0.8                                     |
| 4                | 45.1         | 46.9         | 4.0                                     |
| 5                | 50.9         | 54.2         | 6.6                                     |

Table A.3.: Reliability of the MIR measurements depending on the dissolution step,  $c_t$  - target concentration,  $c_a$  - averaged actual concentration.

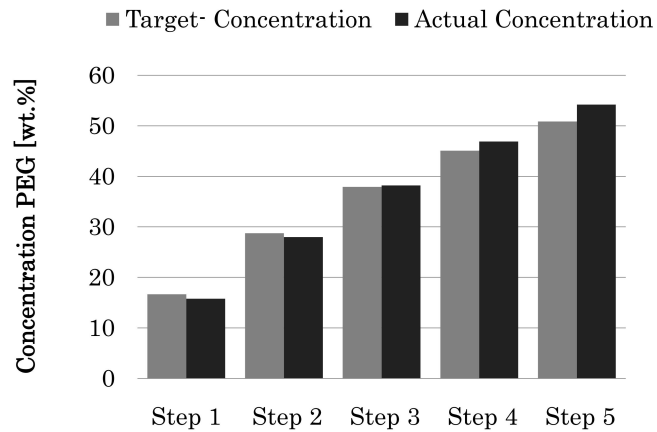


Figure A.5.: Reliability of MIR measurements; comparison of averaged actual and target concentration of the PEG solutions.

## A.4. Solution Properties

### A.4.1. Density

| Concentration PEG<br>[wt.%] | Density<br>[g/ml] |
|-----------------------------|-------------------|
| 0                           | 0.998             |
| 5                           | 1.006             |
| 10                          | 1.015             |
| 15                          | 1.024             |
| 20                          | 1.033             |
| 25                          | 1.042             |
| 30                          | 1.051             |
| 35                          | 1.061             |
| 40                          | 1.071             |

Table A.4.: Densities of the standard solutions of PEG in water.

**A.4.2. Viscosity**

| Concentration<br>PEG [wt.%] | Dynamic viscosity<br>[mPa*s] | Kinematic viscosity<br>[mm <sup>2</sup> /s] |
|-----------------------------|------------------------------|---|
| 0                           | 0.992                        | 0.994                                       |
| 5                           | 2.251                        | 2.237                                       |
| 10                          | 4.382                        | 4.318                                       |
| 15                          | 7.943                        | 7.760                                       |
| 20                          | 13.798                       | 13.356                                      |
| 25                          | 22.094                       | 21.205                                      |
| 30                          | 34.789                       | 33.099                                      |
| 35                          | 55.361                       | 52.198                                      |
| 40                          | 89.258                       | 83.379                                      |

Table A.5.: Viscosity of the standard solutions of PEG in water.

# Bibliography

- [1] K.H. Bauer, K.H. Frömming, and C. Führer. *Lehrbuch der Pharmazeutische Technologie*. Wissenschaftliche Verlagsgesellschaft, 2006. ISBN 3804722229.
- [2] L.T. Borg. Einfluß des Wandmaterials auf das Auslaufverhalten von Schüttgütern aus Silos. *Chemie Ingenieur Technik*, 58(7):588–590, 1986.
- [3] G. Brenn. Stoffübertragung, Vorlesungsskriptum, 2008.
- [4] S. Brunauer, PH Emmett, and E. Teller. Adsorption of gases in multimolecular layers. *Journal of the American Chemical Society*, 60(2):309–319, 1938.
- [5] C.Y. Chang, W.T. Tsai, C.H. Ing, and C.F. Chang. Adsorption of polyethylene glycol (PEG) from aqueous solution onto hydrophobic zeolite. *Journal of Colloid and Interface Science*, 260(2):273 – 279, 2003.
- [6] N.Y.K. Chew and H.K. Chan. Effect of powder polydispersity on aerosol generation. *Journal of Pharmacy and Pharmaceutical Sciences*, 5(2):162–168, 2002.
- [7] LK Doraiswamy and MM Sharma. *Heterogeneous Reaction: Analysis, Examples, and Reactor Design, Vol 2: Fluid-Fluid-Solid Reactions*. Wiley New York, 1984. 233-316 pp.
- [8] J. J. Fitzpatrick, S. A. Barringer, and T. Iqbal. Flow property measurement of food powders and sensitivity of jenike’s hopper design methodology to the measured values. *Journal of Food Engineering*, 61(3):399 – 405, 2004.
- [9] Reg Freeman. Measuring the flow properties of consolidated, conditioned and aerated powders – a comparative study using a powder rheometer and a rotational shear cell. *Powder Technology*, 174(1-2):25 – 33, 2007. Special Edition from the PSA2005 Conference.
- [10] Tim Freeman. *Freeman Technology - FT4 Support Documents*, 2010.
- [11] Barbara Freudig, Stefan Hogeckamp, and Helmar Schubert. Dispersion of powders

- in liquids in a stirred vessel. *Chemical Engineering and Processing*, 38(4-6):525–532, September 1999.
- [12] Drewer G.R., Ahmed N., and G.J. Jameson. An optimum concentration for the suspension of solids in stirred vessels. In *Mixing and crystallization*, pages 83–94. Kluwer Academic, 2000. ISBN 9780792362005.
- [13] P. Guiraud, J. Costes, and J. Bertrand. Local measurements of fluid and particle velocities in a stirred suspension. *Chemical Engineering Journal*, 68(2-3):75 – 86, 1997.
- [14] S. Hogeckamp and M. Pohl. Methoden zur Beurteilung des Befeuchtungs- und Dispergierverhaltens von Pulvern. *Chemie Ingenieur Technik*, 76(4):385–390, 2004.
- [15] R.G. Holdich. *Fundamentals of particle technology*. Midland Information Technology and Publishing Leicestershire, 2002. ISBN 0954388100.
- [16] T. Hörmann, D. Suzzi, and Khinast J. *Mixing and Dissolution Processes of Pharmaceutical Bulk Materials in Stirred Tanks: Experimental and Numerical Investigations*. 2011.
- [17] H.M. Jaeger and S.R. Nagel. Physics of the granular state. *Science(Washington)*, 255(5051):1523–1523, 1992.
- [18] A.W. Jenike. Storage and flow of solids, bulletin no. 123. *Bulletin of the University of Utah*, 53(26):198, 1964.
- [19] Y. Kawashima. *Handbook of Powder Technology Vol. 9 (Powder Technology and Pharmaceutical Processes) ed by D. Chulia, M. Deleuil, Y. Pourcelot*. Elsevier, Amsterdam, 1994.
- [20] J. Khinast. *Pharmaceutical Engineering II: Drug Products and Manufacturing Science, Lecture Notes*, 2010.
- [21] M. Kraume. *Transportvorgänge in der Verfahrenstechnik: Grundlagen und apparative Umsetzungen*. Springer Verlag, 2004. ISBN 3540401059.
- [22] Mariem Lazghab, Khashayar Saleh, Isabelle Pezron, Pierre Guigon, and Ljepša Komunjer. Wettability assessment of finely divided solids. *Powder Technology*, 157(1-3):79 – 91, 2005. 4th French Meeting on Powder Science and Technology.
- [23] A.T.C. Mak. *Solid-liquid mixing in mechanically agitated vessels*. PhD thesis, 1992.

- 
- [24] H. Mollet and A. Grubenmann. *Formulierungstechnik: Emulsionen, Suspensionen, feste Formen*. Wiley-VCH Verlag Weinheim, 2000. ISBN 3527298509.
- [25] R.D. Nelson. *Dispersing powders in liquids*, volume 7 of *Handbook of Powder Technology*. Elsevier Science Publishers B.V., Amsterdam, 1988. ISBN 0444430040.
- [26] E.L. Paul, V.A. Atiemo-Obeng, and S.M. Kresta. *Handbook of Industrial Mixing: Science and Practice*. John Wiley & Sons Inc., 2004.
- [27] K. James Prescott and A. Roger Barnum. On powder flowability. *Pharmaceutical Technology*, 24(10):60–85, 2000.
- [28] Clive A. Prestidge and George Tsatouhas. Wettability studies of morphine sulfate powders. *International Journal of Pharmaceutics*, 198(2):201–212, April 2000.
- [29] M. Rhodes. *Introduction to Particle Technology*. John Wiley & Sons Ltd, 2nd edition, 2008. ISBN 9780470014271.
- [30] O. Scheibelhofer. Combining Rheometric Powder Characterization Techniques with Near Infrared Spectroscopy based on Experimental Design and Multivariate Data Analysis. Master’s thesis, University of Technology, Graz, 2010.
- [31] H. Schubert. Capillary forces - modeling and application in particulate technology. *Powder Technology*, 37(1):105 – 116, 1984.
- [32] H. Schubert and J. Wiley. *Handbuch der mechanischen Verfahrenstechnik*. Wiley-VCH, 2003. ISBN 3527305777.
- [33] Helmar Schubert. Instantisieren pulverförmiger Lebensmittel. *Chemie Ingenieur Technik*, 62(11):892–906, 1990.
- [34] D. Schulze. *Pulver und Schüttgüter: Fließeigenschaften und Handhabung*. Springer-Verlag Berlin Heidelberg, 2nd edition, 2009.
- [35] Dietmar Schulze. Flow properties of powders and bulk solids. Technical Paper from <http://www.dietmar-schulze.de/fre.html> 19.08.2010, 12:59 Uhr.
- [36] Dietmar Schulze. Flow properties of powders and bulk solids and silo design for flow. 2010. Informationsblatt ”Schweddes + Schulze Schüttguttechnik” <http://www.schweddes-und-schulze.de/sssf.html> 17.12.2010, 14:00 Uhr.
- [37] Matthias Stieß. *Mechanische Verfahrenstechnik - Partikeltechnologie 1*. Springer Berlin Heidelberg, 2009.

- [38] Chenhang Sun and John C. Berg. A review of the different techniques for solid surface acid-base characterization. *Advances in Colloid and Interface Science*, 105 (1-3):151 – 175, 2003.
- [39] Sympatec GmbH, System-Partikel-Technik, Am Pulverhaus 1, D-38678 Clausthal-Zellerfeld. *QicPic*, 2009.
- [40] ASI Applied systems. *User's Guide, ReactIR 1000 and ReactIR MP Mobile, Reaction Analysis Systems*. 8223 Cloverleaf Drive Suite 120, Millersville, MD 21108, 3rd edition, 1997.
- [41] N. Urbanetz. Partikelverfahrenstechnik 1, Vorlesungsunterlagen, 2009.
- [42] P.A. Webb and C. Orr. *Analytical methods in fine particle technology*. Micromeritics Instrument Corporation, 1997. ISBN 096567830X.
- [43] C. Wibowo and K. M. Ng. Operational issues in solids processing plants: Systems view. *AIChE J.*, 47(1):107–125, 2001.